STUDY OF A Λ_b^0 DECAY

By

Héctor Andrés Moreno Cano

A thesis submitted in partial fulfillment of the requirements for the degree of

MASTER IN PHYSICS

in

PHYSICS

UNIVERSITY OF PUERTO RICO
MAYAGÜEZ CAMPUS

2014

Approved by:

Dr. Héctor Méndez Mella, Ph.D. President, Graduate Committee	Date
Dr. Juan E. Ramírez Vargas, Ph.D. Member, Graduate Committee	Date
Dr. Samuel A. Santana Colón, Ph.D. Member, Graduate Committee	Date
Dr. Juan Romero, Ph.D. Representative of Graduate Studies	Date
Dr. Rafael A. Ramos, Ph.D. Chairperson of the Department	Date

Abstract of Dissertation Presented to the Graduate School
of the University of Puerto Rico in Partial Fulfillment of the
Requirements for the Degree of Master in Physics

STUDY OF A Λ_b^0 DECAY

By

Héctor Andrés Moreno Cano

2014

Chair: Héctor Méndez-Mella
Major Department: Physics

This thesis shows some results on the study of the Λ_b^0 baryon through the exclusive baryonic decay $\Lambda_b^0 \rightarrow \Lambda^0\psi(2s)$ with the $\psi(2s)$ being reconstructed in the $\psi(2s) \rightarrow \mu^+\mu^-$ decay mode and the Λ^0 in the $p\pi^-$ final state. We worked with 2011 data corresponding to an integrated luminosity of approximatley 5.0 fb^{-1} collected by the CMS experiment at the LHC in pp collissions at $\sqrt{s}$ =7 TeV. The preliminar relative branching fraction B($\Lambda_b^0 \rightarrow \Lambda^0\psi(2s)$)/B($\Lambda_b^0 \rightarrow \Lambda^0 J/\psi$) has been measured to be 0.669 $\pm$ 0.057(stat) $\pm$ 0.043(syst) $\pm$ 0.077(PDG) where the second and third terms are the statistical and systematic uncertainties respectively, and the PDG term is due to the uncertainty in the $J/\psi/\psi(2s)$ branching ratio for the dimuon channel. We also found a preliminar signal measurement of $\Lambda_b^0 \rightarrow \Lambda^0\psi(2s)$ with $\psi(2s) \rightarrow J/\psi\pi^+\pi^-$ decay channel of 165 $\pm$ 67.3 events, MC analysis for its relative branching fraction to confirm the first observation is still in progress.

Resumen de Disertación Presentado a Escuela Graduada
de la Universidad de Puerto Rico como requisito parcial de los
Requerimientos para el grado de Maestría en Física

ESTUDIO DE UN DECAIMIENTO DEL BARIÓN Λ_b^0

Por

Héctor Andrés Moreno Cano

2014

Consejero: Héctor Méndez-Mella
Departamento: Física

Esta tesis muestra resultados preliminares del estudio de el barión neutro Λ_b^0 por medio de el decaimiento bariónico exclusivo $\Lambda_b^0 \rightarrow \Lambda^0\psi(2s)$ donde el mesón $\psi(2s)$ es reconstruido en el modo $\psi(2s) \rightarrow \mu^+\mu^-$ y el barión Λ^0 en el estado final $p\pi^-$. El análisis se realizó con las datos del 2011 correspondientes a una luminosidad integrada aproximada de 5.0 fb^{-1} colectada por el detector CMS en el Gran Colisionador de Hadrones "LHC" (Large Hadron Collider) en colisiones protón-protón a una energía de centro de masa $\sqrt{s}$ =7 TeV. La medida relativa preliminar de el "Branching Fraction" B($\Lambda_b^0 \rightarrow \Lambda^0\psi(2s)$)/B($\Lambda_b^0 \rightarrow \Lambda^0 J/\psi$) (donde el meson J/ψ es reconstruido en el modo de decaimiento $J/\psi \rightarrow \mu^+\mu^-$) resultó ser de 0.669 ± 0.057(stat) ± 0.043(syst) ± 0.077(PDG) en donde el segundo término corres- ponde a la incertidumbre estadística, el tercer término a la incertidumbre sistemática y el cuarto termino corresponde a la del valor nominal (PDG) asociado al "branching fraction" $J/\psi/\psi(2s)$ en el modo de dos muones ($\mu^+\mu^-$). Adicionalmente, se encontró una medida preliminar de la señal de el modo $\Lambda_b^0 \rightarrow \Lambda^0\psi(2s)$ con el mesón $\psi(2s)$ decayendo en $J/\psi\pi^+\pi^-$, de 165 ± 67.3 eventos. Cálculos adicionales y análisis con muestra Monte Carlo (MC) para el "Branching Fraction" en este modo de decaimiento con el fin de confirmar la primera observación estan en progreso.

Copyright © 2014

by

Héctor Andrés Moreno Cano

To God, for giving me his love and for giving me great opportunities.

To my parents, for giving me their love and support.

To my friends and family.

ACKNOWLEDGMENTS

This work has been possible thanks to the collaboration of people during my master who gave me their support.

I give my sincere thanks to:

- My family and relatives, who have given me encouragement, support and love to bring out my projects.

- Dr. Héctor Méndez for the training and support they have given me over the Master in Physics.

- Dr. Eduardo Ramírez and Dr. Samuel Santana for their support and participation in the committee.

- To my colleagues and friends who gave me their support with whom I shared many special moments.

TABLE OF CONTENTS

page

ABSTRACT IN ENGLISH . . . ii

ABSTRACT IN SPANISH . . . iii

ACKNOWLEDGMENTS . . . vi

LIST OF TABLES . . . ix

LIST OF FIGURES . . . x

1 INTRODUCTION . . . 1
- 1.0.1 Standard Model (SM) . . . 1
- 1.0.2 The Higgs boson . . . 5
- 1.0.3 The Large Hadron Collider (LHC) . . . 7

2 THE COMPACT MUON SOLENOID EXPERIMENT (CMS) . . . 10
- 2.0.4 The Electromagnetic Calorimeter (ECAL) . . . 15
- 2.0.5 The Hadron Calorimeter (HCAL) . . . 15
- 2.0.6 The Solenoid Magnet . . . 16
- 2.0.7 The Muon detector system . . . 16
- 2.0.8 The Tracking System . . . 19
- 2.0.9 Strip Tracker . . . 21
- 2.0.10 Pixel tracker . . . 22

3 OBJECTIVES . . . 24
- 3.1 General Objectives . . . 26

4 ANALYSIS . . . 27
- 4.1 Data Sample . . . 27
- 4.2 Event Selection . . . 29
  - 4.2.1 $\mu^+\mu^-$ Selection . . . 30
  - 4.2.2 $\Lambda^0 \to p\pi^-$ Selection . . . 31
  - 4.2.3 Λ_b^0 Reconstruction . . . 33
- 4.3 $\psi(2S) \to \mu^+\mu^-$ Data Analysis . . . 39
  - 4.3.1 $\Lambda_b^0 \to \Lambda^0\psi(2S)$ with $\psi(2S) \to \mu^+\mu^-$ . . . 41
- 4.4 $\psi(2S) \to J/\psi\pi^+\pi^-$ Data Analysis . . . 45
  - 4.4.1 $\Lambda_b^0 \to \Lambda^0\psi(2S)$ with $\psi(2S) \to J/\psi\pi^+\pi^-$ . . . 46
  - 4.4.2 Λ_b^0 Branching Ratio Measurements . . . 49
  - 4.4.3 $\Lambda_b^0 \to \Lambda^0\psi(2S)$ Systematic Uncertainties . . . 52

5 CONCLUSIONS . . . 55
- 5.0.4 Future works . . . 56

5.1 Appendix 57
5.1.1 Appendix A: Λ_b^0 Cross Section Analysis for 2011-A 57
5.1.2 Appendix B: Split Sample (Run 2011 A vs B) 57

LIST OF TABLES

Table page

4–1 2011 Dataset and Luminosities 28

4–2 Λ_b^0 Generated MC branching fraction 29

4–3 Loose $\Lambda^0 \to p\pi^-$ Selection Cuts 32

4–4 $\Lambda^0 \to p\pi^-$ Selection Cuts 34

4–5 $\mu^+\mu^-$ Selection and Λ_b^0 Reconstruction Cuts 35

4–6 Displaced Low Dimuon Mass Trigger (LMT) 42

4–7 Kinematics cuts and LMT matching offline cuts 42

4–8 Number of Events in the $\psi(2S) \to \mu^+\mu^-$ Mode 44

4–9 $\psi(2S) \to J/\psi\pi^+\pi^-$ Reconstruction Cuts 47

4–10 Λ_b^0 Reconstruction cuts in the $\psi(2S) \to J/\psi\pi^+\pi^-$ mode. 49

4–11 Number of Signal Events as a Function of the Dataset. (Sign=S/$\sqrt{S+B}$) 53

4–12 Systematic Uncertainties 54

LIST OF FIGURES

Figure page

1–1 Standard Model particles [1]. 3

1–2 A Feynman diagram considered as a possible process for the production and anihilation of the Higgs [2]. 6

1–3 Exclusion of the Higgs mass range by $b\bar{b}$, ZZ, $\gamma\gamma$ and W's modes [3]. . . 7

1–4 Scheme for the LHC at CERN and its detectors [4]. 8

2–1 Layout of the CMS experiment [5]. 11

2–2 Transversal view of the CMS, according the trayectories that particles produced wether are heavy or soft there are devices to detect them [6]. 12

2–3 CMS orientation coordinates [7]. 13

2–4 Geometrical graphic for the pseudorapidity η in the volume of the CMS detector [8]. 14

2–5 Layout of the solenoid magnet of the CMS [9]. 16

2–6 View of the muon system with its barrel and endcaps [10]. 17

2–7 Transverse view of the caps of the Muon detector structure [11]. 19

2–8 Internal structure of the Tracking system of the CMS [12]. 20

2–9 Transverse view of the Silicon Strip Detector [13]. 21

2–10 Pixel tracker [14]. 22

2–11 Structure of the units of the pixel detector [14]. 23

3–1 J=1/2 baryon representation according to b quark content. 24

3–2 Λ_b^0 Cabibbo favoured decay into Λ^0 and a charmonium state (ψ). 25

4–1 $\Lambda_b^0 \to \Lambda^0\mu^+\mu^-$ decay topology. 30

4–2 $\Lambda^0 \to p\pi^-$ multiplicity (left) and mass (right). 32

4–3 Proton Transverse momentum 34

4–4 Reconstructed invariant mass: K^0_{short} J/ψ (left) and K^0_{short} $\psi(2S)$ (right) in our dataset. A clear B^0 signal is observed which is removed after the Λ_b^0 cuts are applied. 36

4–5 pπ^- (graphics right side) and $\pi^+\pi^-$ (graphics left side) invariant masses for the Λ^0 J/ψ sample (top) and Λ^0 $\psi(2S)$ sample (bottom). The Λ^0 on the right is kept while the K^0_{short} contamination ($|M_{K^0_{short}} - M_{\pi^+\pi^-}|$<20 MeV/c^2) is removed in the final Λ^0_b sample. 37

4–6 B^0 signal (from the data) under the Λ^0_b candidate 37

4–7 Invariant mass for K^0_{short} J/ψ (left) and K^0_{short} $\psi(2S)$ (right). A clear B^0 signal is observed in the MC sample. 37

4–8 Invariant mass for Λ^0 J/ψ (top) and Λ^0 $\psi(2S)$ (bottom). There is not Λ^0_b signal in the B^0 MC sample, the crossfeed is negligible. 38

4–9 Λ^0 $\mu^+\mu^-$ Invariant mass for the 2011 dataset 39

4–10 $M_{\mu^+\mu^-}$ Invariant Mass. 39

4–11 Λ^0 $\mu^+\mu^-$ invariant mass for fitted $\mu^+\mu^-$ as J/ψ or $\psi(2S)$ 40

4–12 Λ^0 $\mu^+\mu^-$ Transverse momentum (left) and Rapidity (right). 40

4–13 $\Lambda^0_b \to \Lambda^0 J/\psi$ or $\Lambda^0_b \to \Lambda^0\psi(2S)$ decay topology. 41

4–14 MC $\Lambda^0_b \to \Lambda^0 J/\psi$ (left) and $\Lambda^0_b \to \Lambda^0\psi(2S)$ (right) signal by trigger path. 43

4–15 Λ^0 $\psi(2S)$ (left) and Λ^0 J/ψ (right) Mass. Top(data) and Bottom(mc). . . 45

4–16 $\Lambda^0_b \to \Lambda^0\psi(2S)$ decay topology with $\psi(2S) \to J/\psi\pi^+\pi^-$. 45

4–17 $M_{\mu^+\mu^-\pi^+\pi^-}$ invariant mass (for $\psi(2s)$ reconstruction). 48

4–18 $\Lambda^0\psi(2s)$ invariant mass for Λ^0_b reconstruction with LMT trigger. 49

4–19 Primary Vertexes Multiplicity for Run 2011 A (left) and B (right). 53

5–1 Relative branching fraction for b baryons (CMS) and meson (PDG). . . . 55

5–2 Run number used in [15] corresponding to a total integrated L=1.8 fb^{-1}. 57

5–3 $\Lambda^0_b \to \Lambda^0 J/\psi$ sample from [15] (left) and this analysis (right). 58

5–4 J/ψ and Λ^0 in this analysis. 58

5–5 $\Lambda^0_b \to \Lambda^0 J/\psi$ sample for Run 2011 A (left) and B (right). 58

5–6 $\Lambda^0_b \to \Lambda^0\psi(2S)$ sample for Run 2011 A (left) and B (right). 59

CHAPTER 1
INTRODUCTION

1.0.1 Standard Model (SM)

Through years, sciences like Physics and Chemistry demonstrate that matter is constitued of several kinds of tiny blocks called elementary particles. All of them are classified by their mass, and interact with others by means of "messenger" particles depending on the force (interaction) they experienced. A scheme of such particles and their phenomenology is provided by the *Standard Model* (SM). It is a theoretical model which explains the interactions (except gravity) that exist between all the known elementary particles that compose the matter up to now according to their physical properties, and shows a framework that gives description to these particles and their corresponding antiparticles according to their intrinsec features that also exist (antimatter). The SM clasiffies these particles according to their intrinsec angular momentum (spin): material particles and the carriers of the interaction. [16]. First, the material particles in the SM have intrinsec angular momentum (spin). The spin's value is half integer 1/2 ($S = \hbar/2$). This value characterizes them as $fermions$ and they are classified in two groups:

<u>*Leptons*</u>: Initially, we have the electron (e) whose mass is 0.511 MeV/c^2, the lightest charged particle. It carries a charge of -1.6$\times$ 10^{-19} C known as the fundamental charge (e). Second, we have the muon (μ^-), heavier than the electron with a mass of 105.65 MeV/c^2 whose charge is e, and the heaviest lepton is called Tau (τ^-) has a mass of 1.77 GeV/c^2 with charge e. They constitute 3 generations of charged leptons.

Another group of leptons neutrally charged are the Neutrinos **($\boldsymbol{\nu}$)** which, were initialy postulated to be founded as an extra-momentum in specific decays being involved in weak interactions [17]. Each kind of neutrinos is associated with the corresponding

charged counterpart $\boldsymbol{\nu_e, \nu_\mu, \nu_\tau}$. Each lepton has its corresponding antiparticle. Then, for instance the positron $\boldsymbol{e}^+$,antimuon $\boldsymbol{\mu}^+$, antitau $\boldsymbol{\tau}^+$ exist, and so do the set of antineutrinos $\boldsymbol{\bar{\nu}_e}$, $\boldsymbol{\bar{\nu}_\mu}$, and $\boldsymbol{\bar{\nu}_\tau}$. In total, we have 12 kind of leptons. The charged ones experience the electromagnetic and weak force, and the neutrinos only experience the weak force.

Quarks: Quarks are fundamental particles. They form groups of two (quark - antiquark) and three (3 quarks or 3 antquarks). ***Baryons*** are the ones of three quarks while the ***Mesons*** are the ones of quark - antiquark. This set of quark composed particles forms the ***Hadrons***. These quarks carry charge that is a fraction of the fundamental charge and a 'color' charge which they let them feel the ***strong*** interaction. The first types of quarks discovered, were the up quark ($\boldsymbol{u}$) with a fraction of the fundamental charge q=2/3 and down($\boldsymbol{d}$) with q=-1/3, composing the first generation of these constituents. They were observed in electron scattering at the SLAC laboratory in the 1960's [16] and considered as constituents of the proton with configuration p(uud) and the neutron n(udd). Later another kind of quarks gave origin to the second generation which emmerged from the proposal of M. Gell-Mann in order to explain the composition of hadrons, which there was the need for explaining other heavier particles, not only in terms of $\boldsymbol{u}$ and $\boldsymbol{d}$ quarks. Then another quark was discovered, and given the name of ***strange*** ($\boldsymbol{s}$) quark with q=-1/3. It was experimentally discovered in 1964. With a lifetime longer from the expected, it was the fact it was given the ***strange*** particle.

Other quark was discovered in 1974 at SLAC's and Brookhaven experiments simultaneously. It was called ***charm*** quark ($\boldsymbol{c}$) with q=+2/3 whose discovery gave the Nobel prize to Burton Richter (SLAC) and Samuel Ting (MIT) [16]. composing with the strange quark the second generation.

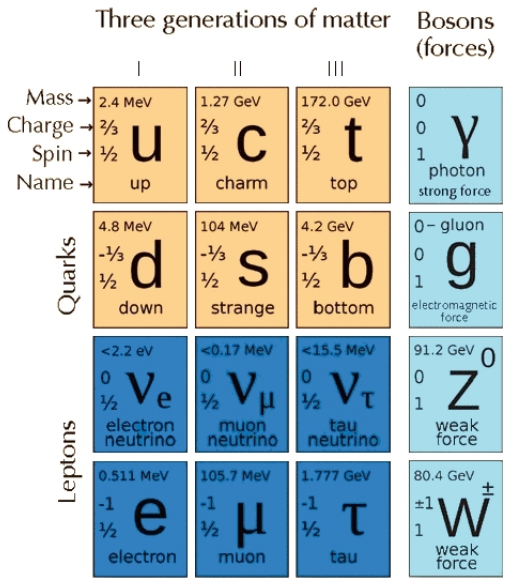

Figure 1–1: Standard Model particles [1].

At the National Laboratory Fermilab in 1977, one of the heaviest quarks in the SM was detected. It was initially labeled by the scientist as the ***beauty*** quark with q=-1/3 but later was given the name of ***bottom*** (***b***) quark. It has a short mean lifetime, because if forms hadrons that decay too soon. A schematic table represents their properties in the Fig 1-1.

The last quark completes the third family and is the heaviest in the SM. It was founded at CDF and D0 experiments at the Tevatron accelerator at Fermilab in 1995. It was given the name the ***top*** (***t***) quark with q=+2/3, and a mass of 176 GeV/c$^{\mathbf{2}}$. Because of its huge mass it makes it an unstable particle, it lasts around $10^{-\mathbf{25}}$ sec. A schematic table represents their properties in the Fig 1-1.

The bottom and top quarks compose the 3rd generation. All off these quarks generate a set of quantum numbers that belong to that the type of quark.

For these 6 quarks, there also exist the set of antiquarks ($\bar{\boldsymbol{u}}, \bar{\boldsymbol{d}}, \bar{\boldsymbol{c}}, \bar{\boldsymbol{s}}, \bar{\boldsymbol{b}}, \bar{\boldsymbol{t}}$).

The SM explains the interaction between particles as a form of exchange of "messenger" particles between material particles, known as the ***force mediators***. Therefore, when a mediator particle of the force is exchanged, it is seen in macroscopic scale as the force exerted over and it is said that the particle has mediated that force. It is understood that the mediators are the reason why the forces exist and the interactions between particles are observed in the universe. The mediators are particles that have integer spin which means that they are ***Bosons***, and there exist a mediator for each interaction.

The ***Electromagnetic*** force, is an interaction mediated by the photon ($\boldsymbol{\gamma}$) that is exchanged between charged particles. The photon is massless and that phenomenology is explained through Quantum Electrodynamics (QED) theory. The quarks also share this interaction because of their charge. The ***Weak*** interactions are mediated by the $Z^{\mathbf{0}}$, W^{+} and W^{-} bosons. They are massive particles, the heaviest is the $Z^{\mathbf{0}}$ with a mass of 91 GeV/$c^{\mathbf{2}}$ and the mass of the W's, is equal to 82 GeV/$c^{\mathbf{2}}$. The W's are electrically charged with the fundamental charge. They mediate the change of flavor for the quarks through a W boson or the generation of a lepton plus its corresponding neutrino as a weak decay [18].

The ***Strong*** interaction takes place in particles with color "charge" and is mediated by gluons ($\boldsymbol{g}$). There are eight types of them being exchanged by the quarks that come in three kinds of color: Red, blue and green. These gluons are neutrally charged and are bicolored , thus in comparison with photons, the gluons can interact between themselves. The phenomenology of quarks and gluons is developed by means of the Quantum Chromodynamics (QCD) theory.

A success of the SM is that, it was able to predict the existence of the boson mediators $W^{\pm}$ and Z, gluons, top and charm quarks before they had been observed, and their physical features had been measured with high precision in the experiments. However, in spite of those achievements, this theory has some limitations. One of them

is the determination of the number of the fundamental physic constants that can't be found independently which is an open question. This model has 19 free parameters that involve quantities such as masses of particles that can be measured by experiment. This model doesn't explain why the different forces operate in such diferent energies. They are manifestations of the same underlying phenomenology, it doesn't explain how they can be unified formally. Some scientists hold the idea that universal laws must come in an ellegant way so what they are looking for is not a change, but a better theory. Such theory could reduce the Standard Model to an approximation, although it could be a step to a "whole theory" [19].

SM It doesn't include the gravitational force because it doesn't describe formally mediators for this interaction to form a quantum theory for gravity similar to the mediators in the SM that are fullfilled in the quantum scale. It means that the particle, known as the gravitron for gravity force hasn't been able to be fullfilled in this model.

SM is a model that agrees with the daily experience to work in four dimensions. In contrast, extra-dimensions theories hold that at least there is an additional dimension for a total of five. Reason which the extras aren't involved in daily living is because they are 'hermetically coiled' that can't be measured with the current technology.

1.0.2 The Higgs boson

The Higgs boson is a massive elementary particle predicted by the SM. This boson has spin 0 and it is an important particle for explaining the generation of mass in the elementary particles. One difference between the massles photon and the masive bosons W's and Z is that the latter have very large masses. These aspects are associated with the postulated new field to produce a kind of interaction that generates the mass. That particle associated is called the ***Higgs Boson*** and the associated field is called the

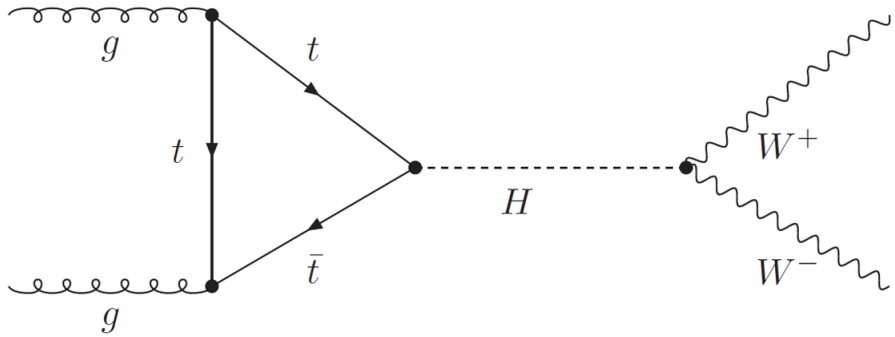

Figure 1–2: A Feynman diagram considered as a possible process for the production and anihilation of the Higgs [2].

Higgs field. This field is in all space but, unlike those known fields, its interaction doesn't produce force between the particles but gives mass to them.

As a measure of the interaction of the particles with the Higgs field, the photon doesn't interact with this field so it does not have mass, but the W's and Z bosons interact stronger with this field and as consequence they have large mass [18].

The Higgs Mechansism [18], was established first theoretically by Peter Higgs, Francois Englert and Robert Brout in 1964. It explains a mechanism that gives mass to the vector bosons and propose that the existence of a scalar massive particle can be a test of such theory. Then, Steven Weinberg and Abdus Salam were the first to apply this mechanism to electroweak spontaneous symmetry breaking, which the electroweak theory predicts a neutral particle whose mass isn't far from the mass of the W and Z bosons.

In spite of the work from the research laboratories at the European Organization for Nuclear Research (CERN) and Fermilab, until the date, the Higgs boson hadn't been observed yet but, beyond that, the data let estimate a minimum experimental value of 114.4 GeV/c$^{\mathbf{2}}$ in the SM, with a confidence level of 95 percent.

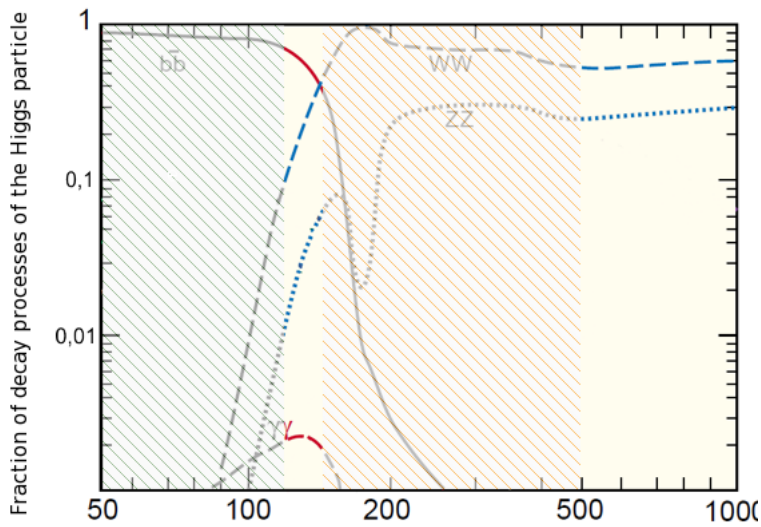

Figure 1–3: Exclusion of the Higgs mass range by $b\bar{b}$, ZZ, $\gamma\gamma$ and W's modes [3].

It was hopefull that Large Hadron Collider (LHC) at CERN, can confirm or deny the existence of this boson [18]. But, in July 2012, results of experiments CMS and ATLAS at LHC at CERN of the search for the Higgs Boson, they found a signal of this particle, with a mass of 125-126 GeV/c^2. Finally, in March 2013 these experiments confirmed that the signal was compatible with Higgs properties, then, it was declared a discovery. Peter Higgs and Francois Englert were given the 2013 Physics Nobel prize for the Higgs boson theoretical discovery.

1.0.3 The Large Hadron Collider (LHC)

The Large Hadron Collider (LHC) is an accelerator and particle collider, the largest experiment in particle physics located at (CERN). It is a two-ring-superconducting hadron accelerator and collider placed in a depth of 100 meters underground and is built in a tunnel of 27 km in circumference. It is a particle accelerator where the physicists study the smallest fundamental particles ever known to examine diverse phenomenology involved after the collisions [20]. For collision supply, there are two transfer tunnels,

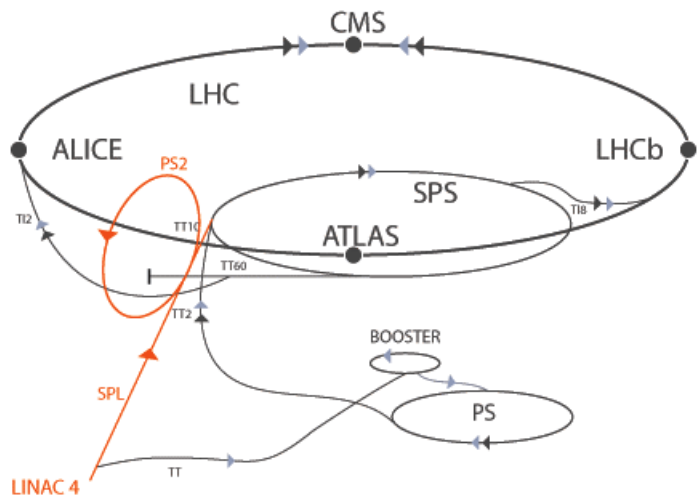

Figure 1–4: Scheme for the LHC at CERN and its detectors [4].

each approximately 2.5 km in length, linking the LHC to the CERN accelerator complex that acts as injector.

The LHC is designed to study the properties of the Standard Model and to has potential for discovering physical signals beyond it. Another aim, was the search for the Standard Model Higgs boson that is a key issue of particle physics. The limits of both collision energy and integrated luminosity are higher in this experiment in one order of magnitude compared to past experiments.

The LHC collides beams of energetic protons moving in opposite directions inside a circular accelerator. These energetic protons reach velocities tending to $0.99999\boldsymbol{c}$ in order to collide and generate other kind of particles that decay into others which are studied. It collides energetic protons at a center-of-mass energy $\sqrt{\boldsymbol{s}}$= 8 TeV in packets (bunches) in periods of 25 ns. It runs at a luminosity aproximately of $10^{\mathbf{34}}$ cm$^{-\mathbf{2}}$s$^{-\mathbf{1}}$ and an intergrated luminosity of 100 fb$^{-\mathbf{1}}$/year that produces $10^{\mathbf{9}}$ events per second about 20 interactions each time 2 bunches collide. With the purpose of studying these collisions, LHC is composed of four experiments which will let analyze and reconstruct events to

study properties of the emergent particles. A diagram of the LHC is displayed in figure 1-2 [21]. One of these experiments in the LHC is the Compact Muon Solenoid (CMS). The CMS is a general-purpose detector that collides proton beams and operates at a luminosity of 10^{34} $cm^{-2}s^{-1}$ whose aim is to study physic aspects of the collisions in the TeV energy order, the search of the Higgs boson, study heavy ions, pursuit phenomenology beyond the Standard Model such as extra-dimensions, dark matter, and supersymmetry. Another experiment that handles this luminosity is A Toroidal LHC Apparatus (ATLAS). It is a multi-purpose detector too, that goes for the production and indirect properties of the B mesons, the research of the CP violation, known as an assymetry between matter and antimatter whose experiments hasn't detected such violation in the SM to explain the lack of anti-matter in the universe.

There are experiments that run at LHC at low luminosity (10^{32} $cm^{-2}s^{-1}$). They are the Large Hadron Collider Beauty (LHCb), speciallized in studying the properties of the b quark and also the measurement of parameters of the CP violation in the hadron desintegrations that contain such quark or the branching ratios of unusual processes in the interaction point of the collision of protons. Pairs of top and anti-top quarks will be produced that later will form particles through the hadronization process. The total cross section elastic scattering and diffraction dissociation measurement (TOTEM) experiment is dedicated to the precise measurement of the proton-proton cross section and the deep study of the proton structure that is barely understood [21].

A Large Ion Collider Experiment (ALICE) is one of the six detectors that is employed for the study of the heavy-ion-collisions where Pb-Pb nuclei are examinated, working at a center-of-mass energy of 2.7 TeV per nucleon to reach conditions of temperature and energy high enough to produce the quark-gluon plasma, a state of the matter where quarks and gluons can be decoupled.

CHAPTER 2
THE COMPACT MUON SOLENOID EXPERIMENT (CMS)

The Compact Muon Solenoid (CMS) is a general purpose detector to study the wide range of particles and phenomena produced in the high-energy collisions in the LHC [22]. It is designed to study head-on proton-proton collisions in beams with a center of mass energy of 8 TeV and a luminosity of 10^{34} $m^{-2}s^{-1}$. The CMS has a cilyndrical shape, with 15 m in diameter, weights 12500 tons and has a lenght of 21.6 m, a scheme for the CMS is shown in fig 1-3. Its main distinguishing features are the high-field solenoid to bend the emerging charged particles, a silicon based inner tracking system, the homogeneous system of scintillating crystals based electromagnetic calorimeter and the four integrated muon detector stations to ensure robustness and full geometric coverage for outgoing muons. For an optimus detection performance, some of relevant purposes are planned for CMS [20]:

• Work in the particle collisions in a higher range of energy imposed on the particles (TeV), which operates at $\sqrt{s} = 14$ TeV and reaches a luminosity of 10^{34}/ cm^2 s). The fact that it has higher energy ion beams than other present day accelerators in other experiments in the world will allow it to perform unique studies of nuclear matter.

• Search beyond the phenomenology in the branches of the SM, such as the search of extra dimensions, supersymmetry, etc. that can lead in some way to have insight of unifcation theories.

• Make a deeper study in the collisions of heavier particles due to the short lifetime that characterizes them.

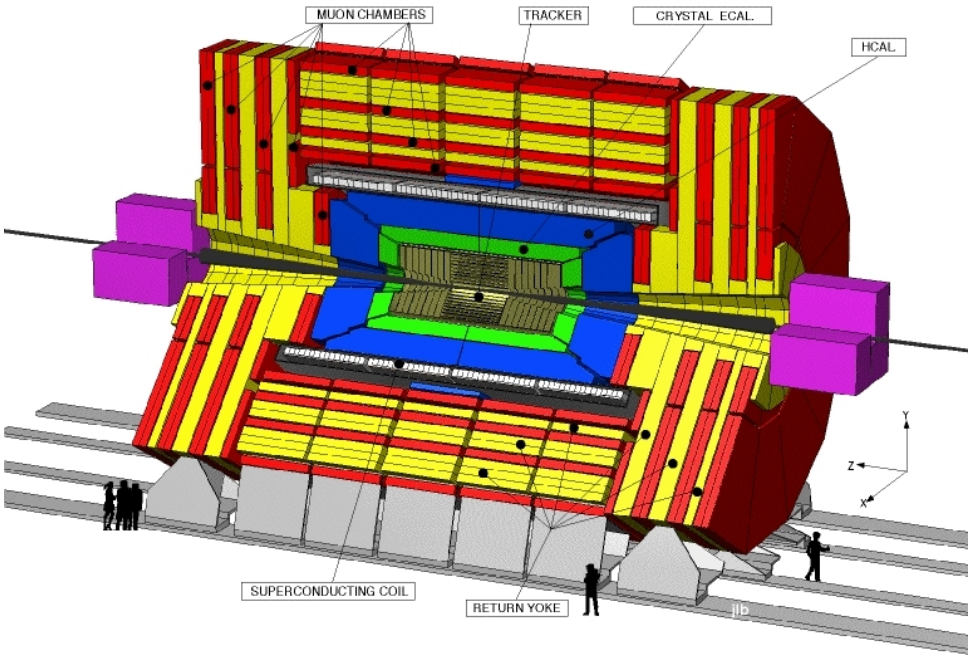

Figure 2–1: Layout of the CMS experiment [5].

The CMS detector is provided with state-of-the-art devices for measuring the energy and the momentum of the emerging particles that are product of the primary collisions, such as muons, photons, mesons, etc [23].

As mentioned, the innermost structure begins with a tracker layer made of semi-condutor materials. The next section is a composed set of crystals scintillators called Calorimeters, this one is employed to detect particles that obey the electormagnetic interactions, this is called the Electromagnetic Calorimeter. This is followed by another calorimeter that detects several kind of emerging hadrons called Hadron Calorimeter [24]. A magnet given by a soleniod produces a high-strenght magnetic field that reaches a field magnetic magnitude of 4 T, that solenoid covers the tracker and the calorimeters and outside it there is the zone of the muon detectors, the devices that make the CMS suitable to detect muons [20].

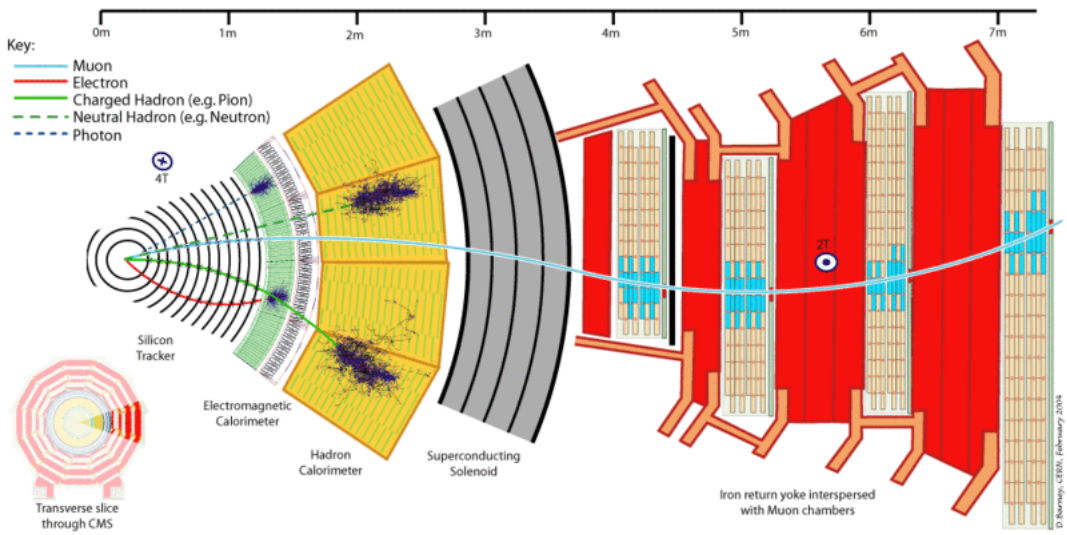

Figure 2–2: Transversal view of the CMS, according the trayectories that particles produced wether are heavy or soft there are devices to detect them [6].

In the central zone of the collisions, the energetic protons are focused by means of magnet systems from LHC, that forces them to collide in the center of the detector. When a pair of energetic protons collide, there is an exchange of mass and energy takes place generating many kind of particles under study. Some of them live longer than other, some are heavier than others, other kinds decay into 2 or more constituents. These protons come distributed in "bunches" with an estimated of $10^{\mathbf{5}}$ million of them, in those amounts, with a rate of 20 collisions per 200000 million protons, and is estimated that 100 from $10^{\mathbf{9}}$ millions of collisions will produce events of important studies. That is why it is important for CMS to produce as many collisions as posible and the advantage of working with the bunches traveling so close in the incident beam in some $10^{\mathbf{9}}$ inelastic events per second [25].

After collisions, the emerging particles move in all directions to the diferent section of the detector, thus, an orientation is adopted in the way they use coordinates such that the center is located in the main zone of the collisions. The x coordinate is taken to be

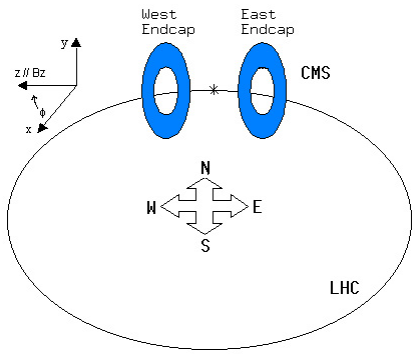

Figure 2–3: CMS orientation coordinates [7].

radially inward the center of the LHC, the y direction going upward and the z direction goes alongside the axis of the experiment.

As usual, the momentum for an emerging particle is described in terms of its components in the x, y and z axis whose magnitude is as follows

$$|\overrightarrow{p}| = \sqrt{p_x^2 + p_y^2 + p_z^2} \tag{2.1}$$

The azimutal angle ϕ is taken from the x axis to be contained in the xy plane. The polar angle θ is contained in the yz plane. Then, an apropiate spacial quantity is used for the outgoing particles, it is called pseudorapidity (η). It is used to describe the direction of a particle related to the beam axis and is given by [26]:

$$\eta = -ln(tan(\frac{\theta}{2})) \tag{2.2}$$

the argument θ is the angle subtended between the momentum of the particle $\overrightarrow{p}$ and the direction of the beam axis, it can also be expressed in terms of the logitudinal component of the momentum (p_L):

$$\eta = -ln(\frac{|\overrightarrow{p}| + p_L}{|\overrightarrow{p}| - p_L}) \tag{2.3}$$

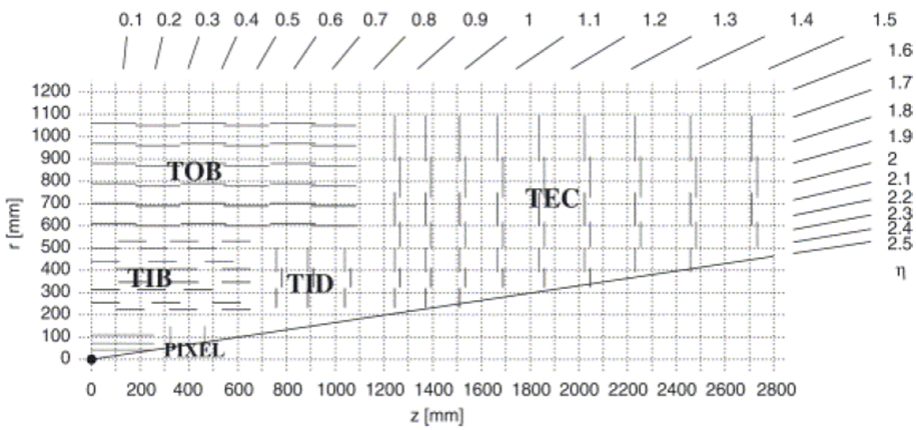

Figure 2–4: Geometrical graphic for the pseudorapidity $\boldsymbol{\eta}$ in the volume of the CMS detector [8].

$$\boldsymbol{y = -ln(\frac{E + p_L}{E - p_L})} \tag{2.4}$$

However, pseudorapidity depends only on the polar angle of its trajectory, and not on the energy of the particle. In hadron collider physics, the rapidity (or pseudorapidity) is preferred over the polar angle $\boldsymbol{\theta}$ because, loosely speaking, particle production is constant as a function of rapidity. One speaks of the "forward" direction in a hadron collider experiment, which refers to regions of the detector that are close to the beam axis, at high $|\boldsymbol{\eta}|$ [26].

Another important physical quantity for emerging particles is the transverse momentum, whis is the projection of the total momentum $\overrightarrow{\boldsymbol{p}}$ in the CMS xy plane.

$$\boldsymbol{p_T = \sqrt{p_x^2 + p_y^2}} \tag{2.5}$$

It is relevant because the momentum along the beamline may just be left over from the beam particles, while the transverse momentum is always associated with whatever physics happened at the vertex.

2.0.4 The Electromagnetic Calorimeter (ECAL)

An instrument that works for receiving amounts of energy given by particles, the Electromagnetic Calorimeter is an homogeneous device that is compounded by 62,500 lead tunsgstate ($PbWO_4$) scintillators crystals located in the central barrel zone and enclosed by 7324 crystals in the 2 outer endcaps that work in a range of pseudorapidity up to $|\eta| < 3.0$. The scintillation light is detected by silicon avalanche photodiodes (APDs) in the barrel region and vacuum phototriodes (VPTs) in the endcap region. That can mainly measure with high precision the energy of the emerging photons and electrons that feel that kind of interaction. Its silicon sensors detectors have the abilty to identify the particle in its external caps.

2.0.5 The Hadron Calorimeter (HCAL)

The HCAL is a detector that can determine the energy of the hadrons that pass through, such barions like protons or neutrons, mesons like kaons or pions. The HCAL is composed of a set of layers of scintillators tiles that are located in the quarz fiber that cover the range -1.26 $< \eta <$ 1.26 at the hadron outer zone, the hadron barrel consisting of 32 towers that cover -1.4 $< \eta <$1.4 , the Hadron endcap zone formed by endcaps each formed by 14 towers covering the -1.3 $< \eta <$ 3.0 region and the Hadron forward zone made of steel/quarz-fiber calorimeters that cover 3.0 $< \eta <$ 5.0 [24].

The material which this is made of is brass. Such a metal is non-magnetic, whose advantages are that it is a good particle absorber and has short interaction lenght for the incident particles. This device is located inside the magnet coil surrounding the ECAL system.

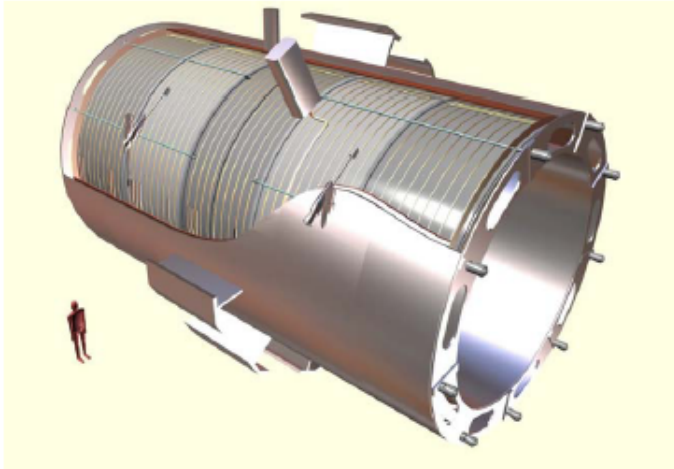

Figure 2–5: Layout of the solenoid magnet of the CMS [9].

2.0.6 The Solenoid Magnet

As a common feature in particle detectors, the CMS has a large supercondcting solenoid magnet, that operates at 3.8 T with a great performance to bend the emergent charged particles specially to measure the momentum of muons.

It has a lenght of 12.9 m and a free bore that has diameter of 6 m and a weight of 220 tons. It has a NiTi core that is constantly refrigerated with liquid helium to keep superconducting conditions. The bore of that magnet coil is enough to contain the inner tracker and the calorimeters inside. The Solenoid Magnet is the device around which the components of CMS are build. It has the conditions to keep an uniform field alongside the axis of the track, its strenght stores an energy of about 2.7 GJ when operating a current of 19.5 kA.

2.0.7 The Muon detector system

The muon detection is an important tool to recognize signatures of processes which, in their decay processes generate leptons, specially if they are muons. For this reason,

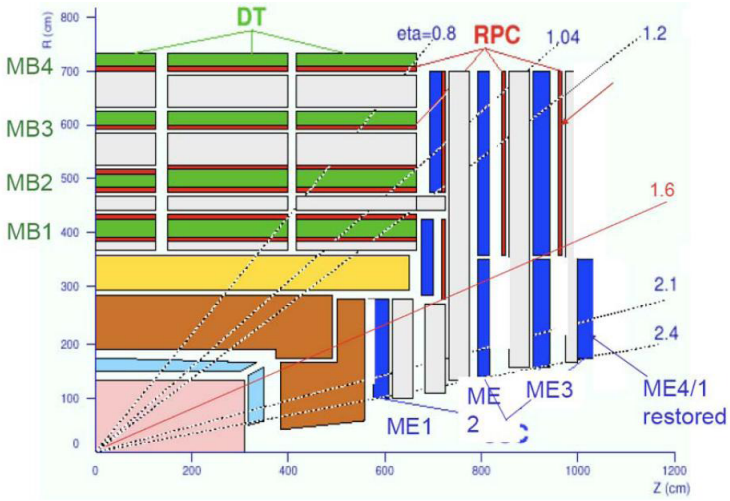

Figure 2–6: View of the muon system with its barrel and endcaps [10].

the detection of muons is of great importance for the CMS and a precise and robust muon measurement was an aspect of the design. That is why the muon system develops three functions: The muon identification, momentum measurement and triggering. The high field solenoid magnet provides good momentum resolution and triggering ability, and the flux return yoke works as a hadron catcher to enhance the muon identification.

Muons produced in such collisions are measured in three zones, in the inner tracker, outside the solenoid and the return flux zones. The aim of the measurement of momentum that the muons carry is provided by the bending effect of the coil. The resolution of the measurements is set by multiple scattering in the material to the muons with momentum in the range of $p_{\boldsymbol{T}} = 200$ GeV/c. For the muons that carry low amount of momentum the resolution is taken at the silicon tracker located in the inner tracking system. However, the muon trajectory beyond the return yoke extrapolates back to the beam line due to the compensation of the bend before and after the coil when multiple scattering and energy loss can be neglected. This fact can be used to improve the muon

momentum resolution at high momentum when combining the inner tracker and muon detector measurements, the pseudorapidity in the barrel is up to $\eta < 0.8$ and at the endcap is between $1.8 < \eta < 2.0$ [24].

This muon system has the ability to reconstruct the charge and momentum of muons. That is the purpose for CMS to use three types of particle detectors to identify the muons. Its shape has a cilyndrical barrel section and two planar endcap regions and covers an area of detection of 25,000 m^2 in form of detection planes. The first type of detector is the drift chambers located alongside the barrel region. The barrel drift tube chambers (DT) cover the region of pseudorapidity $|\eta| < 1.2$. They are detectors for high precission measurements of the track in the inner barrel and are divided into four stations, the first three contain eight chambers, distributed in two gropus of four which can measure the muon coordinate in the $r - \phi$ plane. For the bending region they are separated as much as they can to achieve the best angular resolution, and the other four chambers provide a measurement alongside the beam line (z direction), and the fourth station doesn't include the z region coverage [20].

In the two endcaps of the detector the magnetic field is not uniform and has a large intensity rate of muons. In such configuration and conditions the muon system uses cathod strip chambers (CSC) which identify muons in the the pseudorapidity domain $0.9 < \eta < 2.4$. Similar to the configuration of the DT that region is organized in four stations of CSC in each endcap with their respective chambers positioned perpendicular to the beam line. The strips of each chamber point out radially outward and have a precision measurement in the $r - \phi$ bending plane. The CSC posess good recognition for rejection of non-muon backgrounds and efficient matching of hits.

There is a complementary system of muon triggering that consists of resistive plate chambers (RPC) that are added to the barrel and endcap regions of the detector. This kind of chambers provides an optimal triggering with a sharp p_T threshold over a large

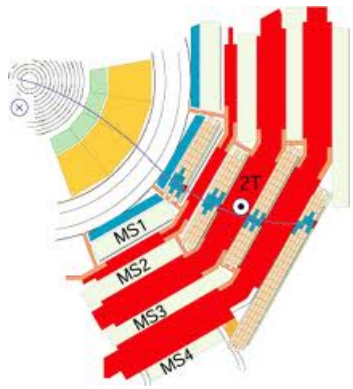

Figure 2–7: Transverse view of the caps of the Muon detector structure [11].

portion of the rapidity range $|\eta| < 1.6$ of the muon system. They are double-gap chambers, operated in avalanche mode to ensure good operation at high rates, with fast response and good time resolution, they identify ambiguities with respect to make tracks from multiple hits in a chamber. They are distributed in six layers embedded in the barrel muon system, two are located in each of the first two stations that allow ease to the trigger to work even in the low p_T tracks and one in each of the last two stations. In the endcap region there is a plane of RPC in each of the first of the DT that helps the trigger to reduce background, improve time resolution for bunch crossing identification and for achievement of a good p_T resolution.

2.0.8 The Tracking System

In order to observe the phenomenology that occurs at the collsions, the CMS experiment is provided with a complete system of measurement and detection that allows to look inside the products coming from those decays and interactions of the particles that occur in the vertexes at high energies, which are mostly charged or neutral particles that underline a kind of dynamics at the inner region of interest. The tracker consists of a central (barrel) part with three pixel and ten strip layers and the disk and endcap sections with two pixel and twelve strip layers.

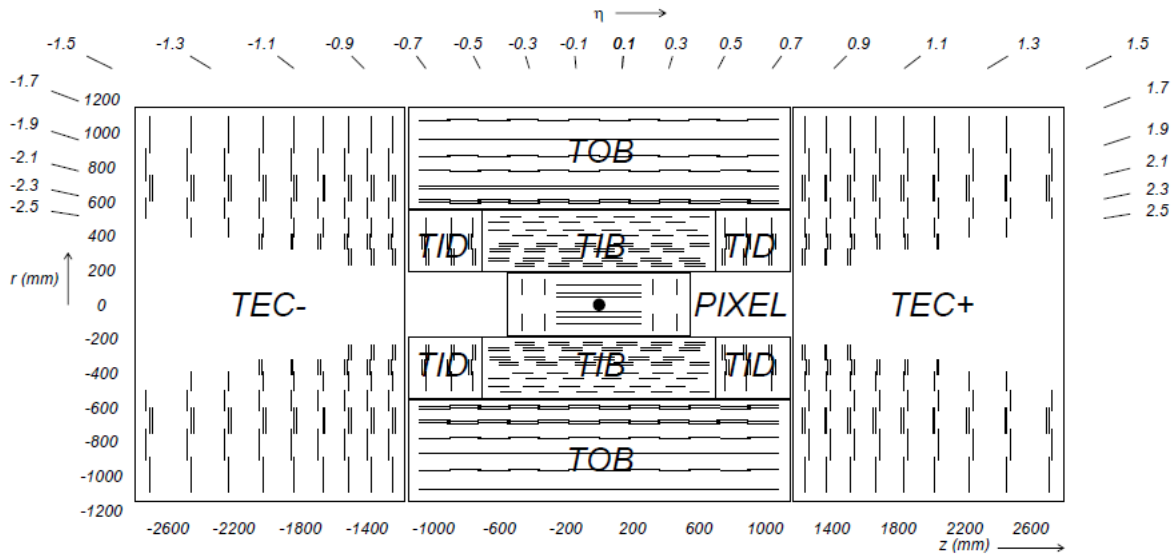

Figure 2–8: Internal structure of the Tracking system of the CMS [12].

A system of pixel detectors is located at the closest zone to the vertex where a high flux of particles is reached (10^7 events/sec). The dimensions of each pixel are about 100 $\times$ 150 μm^2, in the next region, from 20 to 55 cm, there are silicon microstryp detectors of in layers if 10 cm $\times$ 80 μm. It is a region where the particle flux decreases considerably. At a radial distance more than 55 cm (as far a radial distance of the traker of 110 cm), where the flux is notably reduced, there are silicon strips are of a minimum size of 25 cm $\times$ 180 μm.

A scheme of the tracking system is shown with their inner and outer detectors. In the barrel region close to the initial vertex there are 3 layers of pixel detectors located at radial distances of 4.4, 7.3 and 10.2 cm, in the barrel zone, the silicon detectors are placed between 20 and 100 cm.

The forward region has 2 pixels and 9 microstrip layers in each of the 2 endcaps. The barrel part is compounded in an Inner Barrel and Outer Barrel. The Inner Barrel is

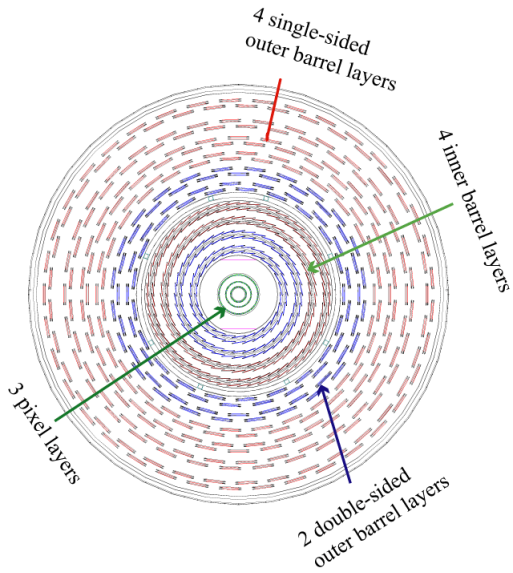

Figure 2–9: Transverse view of the Silicon Strip Detector [13].

placed in a shorter distance than the outer one to avoid excessive track crossing angles. Also there are an additional 3 Inner Disks in the region between the barrel and endcap on each side of the Inner Barrel. The total area of the pixel detector is ≈ 1 m^2 [23], the silicon strip detectors area is 200 m^2, providing coverage up to $|\eta| < 2.4$. The inner tracker comprises 66 million pixels and 9.6 million silicon strips.

2.0.9 Strip Tracker

The Silicon Strip Tracker (SST) subtends an area of 206 m^2, which makes it the largest silicon ever built, the sensors are in array in a total number of about 20,000 modules, which consist of one or two strip detectors placed in series together with the associated readout electronics features. The geometry of the sensors and the number of readout strips varies whether they could be located: In the barrel region the sensors are rectangular, while the endcap sensors are of trapezoidal shape to fit together in discs [23].

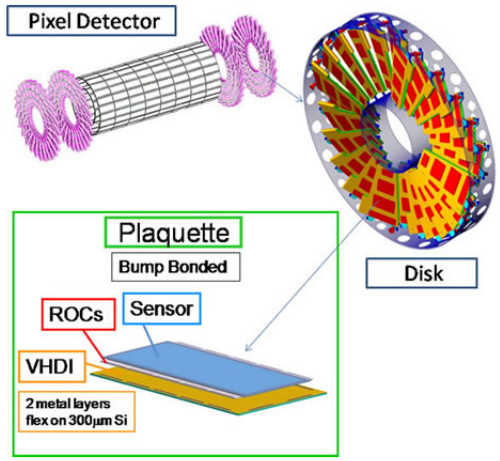

Figure 2–10: Pixel tracker [14].

Ten strip layers in the barrel are divided into the Inner Barrel (IB) and the Outer Barrel (OB), which are numbered in ascending order according to the radius. Seven rings of the disk modules are divided into the Inner Disks (ID) and the Endcaps (EC), also numbered according to ascending radius.

The barrel modules will be placed on the surface of cylindrical support structures, To allow better area coverage, the modules will overlap like roof tiles, which causes a tilt angle of 9° to 12° out of the tangential plane.

2.0.10 Pixel tracker

The high resolution pixel detector is the innermost part of the CMS Tracker. Since the particle density is very high, a small scale pixel geometry is required for unambiguous hit recognition and precise vertex reconstruction. Short-lived particles arise from the primary vertex, which can decay after having travelled only a few hundred micrometers.

The pixel detector distinguishes such secondary vertices from the original collision point. It is composed of 3 barrel layers and 2 endcap disks located at each side. They have a lenght of 53 cm, the disks are located at a radii of 4.4 cm, 7.3 cm and 10.2 cm.

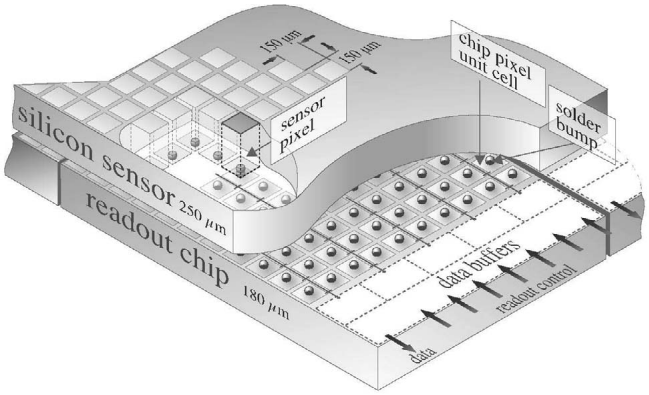

Figure 2–11: Structure of the units of the pixel detector [14].

The disks form 6 to 15 cm in radius, and they are placed on each side at a height |z| = 34.5 cm and 46.5 cm [23].

To get the optimal vertex position resolution, there is a design with an similar square pixel shape of 100 $\times$ 150 $\boldsymbol{\mu}\mathbf{m}^{\mathbf{2}}$ in a system of cilyndrical coordinates r, $\boldsymbol{\theta}$,z as system location. The barrel comprises 768 pixel modules arranged into half-ladders of 4 identical modules each, and the endcap disks contain 672 joint pixel modules with 7 modules in each cap.

CHAPTER 3
OBJECTIVES

Hadrons are bound systems of particles, bounded by the strong interaction. They are described at the fundamental level by quantum chromodynamics (QCD). It is well understood that in high energy phenomena, it is difficult to predict binding of quarks and gluons within hadrons. Several models and techniques, such as constituent quark models or lattice QCD calculations, attempt to reproduce the spectrum of the measured hadron masses [27]. The quark model classifies baryons with a representation of spin J=1/2 or J=3/2 [28].

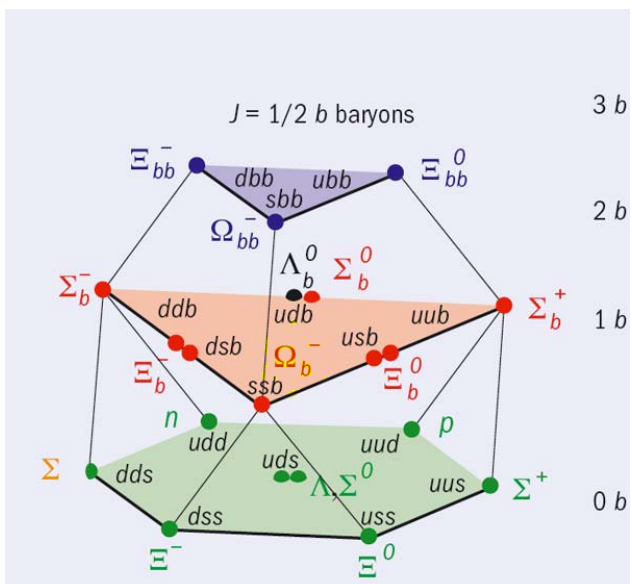

Figure 3–1: J=1/2 baryon representation according to b quark content.

In the figure 3–1, of the three levels of states of baryons, the middle level represents a family of the $\mathbf{\Lambda}$ baryons containing one b quark in its structure. These baryons contain contain b-quarks and among these only the lowest lying state has been observed at Fermilab Tevatron collider and LHC at CERN. For this baryon, the theoretical predictions

for the mass, are in the range 5.547 - 5.660 GeV/c$^{\mathbf{2}}$. It is a neutral protonlike baryon containing a b quark (udb). It has a mean lifetime of $1.383^{+\mathbf{0.049}}_{-\mathbf{0.048}}$ x $10^{-\mathbf{12}}$ sec. Progress in understanding, the weak decays of bottom baryons has been very slow and scarce in both theoretical and experimental front. While some new data of charmed baryon nonleptonic weak decays has become available, $\boldsymbol{\Lambda_b^0} \rightarrow \boldsymbol{\Lambda}$ J/$\boldsymbol{\psi}$ is one measurement of the exclusive hadronic decay rate of bottom baryons. In the near future, one can expect new data on exclusive bottom baryon decays, calling for a comprehensive theoretical analysis of these decay modes. These decay processes can provide useful information on QCD effects in weak decays and indirect CP asymmetry.

An approach applied successfully to nonleptonic B meson decays can also be applicable to phenomenology of bottom baryon decays. Only few $\boldsymbol{\Lambda_b^0}$ baryon decay channels have been examined with enough precision due to low experimental statistics. The uncertainty in branching fraction of $\boldsymbol{\Lambda_b^0}$ decays channel varies over a range (10% - 70%). At the Large Hadron Collider (LHC), with high luminosity and energy, b hadrons become more experimentally accesible. We can then measure their phyisical properties such as lifetime, polarization, CP and T violation, with an improved precision. Also making possible the observation of new b baryon states and, their corresponding decay modes.

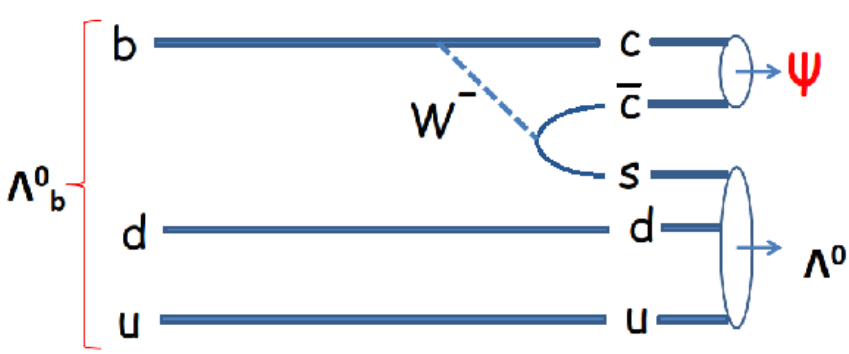

Figure 3–2: $\boldsymbol{\Lambda_b^0}$ Cabibbo favoured decay into $\boldsymbol{\Lambda^0}$ and a charmonium state ($\boldsymbol{\psi}$).

The Λ_b^0 decay channel of interest to us involves a change of flavor of the b quark to an s and anti-c quarks through a weak current (W^- boson), where the quarks u,d and s form the Λ^0 and the c and anti-c quarks form the ψ state that can be either the J/ψ or $\psi(2s)$.

3.1 General Objectives

This thesis is intended to study exclusive hadronic decay $\Lambda_b^0 \to \Lambda^0\psi(2S)$ where $\psi(2S)$ meson decays to $\mu^+\mu^-$ and Λ^0 to $p\pi^-$. The analysis is carried with the data recorded by the CMS experiment in 2011 in pp collisions at the center-of-mass energy $\sqrt{s}$ = 7 TeV with an integrated luminosity of 5.0 fb^{-1}. We want to calculate the branching fraction B($\Lambda_b^0 \to \Lambda^0\psi(2S)$) relative to the one normalizing channel B($\Lambda_b^0 \to \Lambda^0 J/\psi$) with $J/\psi \to \mu^+\mu^-$. In addition, we want to confirm the $\Lambda_b^0 \to \Lambda^0\psi(2S)$ decay with $\psi(2S) \to J/\psi\pi^+\pi^-$ in order to make a confirmation of the previous observation.

The data is used in this analysis has a wide sample of muon events, where we make the initial reconstruction process for the J/ψ and $\psi(2S)$ mesons where the dimuon pairs ($\mu^+\mu^-$) come from. For better signal processing and reconstruction of the Λ_b^0, these muon candidates are required to match a set criteria from a muon selection system. Pion and proton events are used to reconstruct the Λ^0 baryon through $\Lambda^0 \to p\pi^-$ decay. The particle candidates which are useful for reconstructing each hadron are clasified according to a selected criteria represented in selection of values for momentum, transverse momentum, pseudorapidity, etc.

To provide an agreement with what is found in data analysis, Λ_b^0 Monte-Carlo (MC) samples are produced and analyzed in similar way. This involves several steps which pass generated physical processes through a simulation of the detector and allows to see what new physics would look like when seen by the detector and hence where to concentrate the search in order to select parameters and estimate reconstruction efficiencies.

CHAPTER 4
ANALYSIS

4.1 Data Sample

This analysis uses an integrated luminosity of 5.0 fb^{-1} recorded by the CMS experiment at the LHC during 2011 with pp collisions at the centre-of-mass energy of $\sqrt{s} = 7$ TeV. In this work, the Λ_b^0 is reconstructed in both, the signal $\Lambda_b^0 \to \Lambda^0\psi(2S)$ and the normalizing $\Lambda_b^0 \to \Lambda^0 J/\psi$ mode. The $\psi(2S)$ meson is reconstructed in the $\mu^+\mu^-$ decay channel ($\psi(2S) \to \mu^+\mu^-$) as well as the J/ψ ($J/\psi \to \mu^+\mu^-$) and Λ^0 reconstructed into pπ^- ($\Lambda^0 \to p\pi^-$). The data is collected by the detector and then it becomes mandatory to use a trigger system in order to select events according to physics-driven choices. The CMS experiment features a two-level trigger architecture. The first level (L1), hardware, operates a first selection of the events to be kept, using muon chambers and calorimeter information. The maximum output rate from L1 is about 100 kHz; this upper limit is given by the CMS data acquisition electronics. The second level, called High Level Trigger (HLT), is implemented in software and aims to fur- ther reduce the event rate to about 800 Hz on average. Events passing the HLT are then stored on local disk or in CMS Tier-0; about a half of these events were promptly reconstructed, while the other half have been parked and then reconstructed.

From there, the HLT paths are designated to live inside a specific "Primary dataset" (PD). PD's are distributed in entirety to T1's and T2's, so accessing them is the primary mode that you will be using to access the data..

The dimuons ($\mu^+\mu^-$) contained in the final state, were extracted from the enriched dimuon skim called "MuOnia" dataset (Table 4–1). where Analysis Object Data (AOD) a subset of reconstructed data RECO which contains only high-level objects which should be suficient for most analysis. The group of datasets have similar characteristics, like

experiment software release (CMSSW), creation time and the skim MuOnia from primary datasets.

The muons from the signal and from the normalization modes are required to match at the same time the dimuon High Level Trigger (HLT). In this analysis we use the displaced low dimuon mass trigger (LMT) which is a trigger path that covers both resonances J/ψ and $\psi(2S)$.

Table 4–1: 2011 Dataset and Luminosities

Dataset	L (pb^{-1})
/MuOnia/Run2011A-PromptReco-v4/AOD	999.5
/MuOnia/Run2011A-05Aug2011-v1/AOD	437.3
/MuOnia/Run2011A-PromptReco-v6/AOD	721.7
/MuOnia/Run2011B-PromptReco-v1/AOD	2891.0

The evolution of the LMT is very well described in reference [29] in the CMS B-Physics trigger in reference [30].

Our analyzer uses PAT (Physics Analysis Tool) objects. PAT is a high-level analysis layer providing the Physics Analysis Groups (PAGs) with easy access to the algorithms developed by Physics Objects Groups (POGs). It aims at fulfilling the needs of most CMS analyses, providing both ease-of-use and flexibility for users.

It is used to extract and analyze the Λ_b^0 sample in addition to match the HLT. The CMSSW_4_2_8_patch7 was used in this work. The good runs were selected based on information on which luminosity sections in which runs are considered good and should be processed is collected in certification files that are in JSON format and are released weekly by the Certification Team. They were selected with the "***MuonPhys***" JSON file:

$$\boldsymbol{Cert_160404-180252_7TeV_PromptReco_Collisions11_JSON_MuonPhys.}$$

An official CMS Monte Carlo (MC) simulated signal event sample* is used to tune the selection criteria, check the agreement with data, compute the acceptance, and derive the Λ_b^0 reconstruction efficiency.

Table 4–2: Λ_b^0 Generated MC branching fraction

Decay Mode	branching fraction
B($J/\psi \to \mu^+\mu^-$)	1
B($\psi(2S) \to \mu^+\mu^-$)	0.1741
B($\psi(2S) \to J/\psi\pi^+\pi^-$)	0.4762
B($\Lambda_b^0 \to \Lambda^0 J/\psi$)	0.168
B($\Lambda_b^0 \to \Lambda^0\psi(2S)$)	0.053
B($\Lambda^0 \to p\pi^-$)	0.6390

4.2 Event Selection

The pp colisions that take place in the CMS experiment generate emerging particles which travel along the detectors. These leave traces (called tracks) in the detector components as hits. In this way the particle trajectory is reconstructed with the set of hits, and therefore it helps to determine its identification, charge and momentum. The CMS experiment possess an optimal system for muon identification.

The analysis strategy consisted of first reconstructing the dimuon pair. Then look for another pair of tracks corresponding to $\Lambda^0 \to p\pi^-$ candidate. Once the $\mu^+\mu^-$ and the Λ^0 candidates are found, we reconstruct a "loose" Λ_b^0 sample by computing its invariant mass (Fig. 4–9) using a three-body reconstruction and then begin the analysis by examining the underlying $M_{\mu^+\mu^-}$ mass distribution in the selected sample.

* /LambdaBToPsiMuMu_2MuPEtaFilter_Tight_7TeV-pythia6-evtgen/Fall11-HLTBPh2011_START42_V14B-v2/GEN-SIM-RECO

Adittionally, be able to make a reconstruction of the $\Lambda_b^0 \to \Lambda^0 J/\psi$ decay channel, being our normalization mode. The decay event topology of these two cases ($\Lambda_b^0 \to \Lambda^0 \psi(2S)$ and $\Lambda_b^0 \to \Lambda^0 J/\psi$) are similar. They are sketched in Fig. 4–1.

This work closely follows a previous CMS study [15] on $\Lambda_b^0 \to \Lambda^0 J/\psi$ cross section measurement using displaced J/ψ triggers in the run 2011-A dataset. Applying in our analysis program the same set of cuts they used to extract the $\Lambda_b^0 \to \Lambda^0 J/\psi$ signal, we were able to reproduce its main distributions, such as the J/ψ, Λ^0 and the $\Lambda_b^0 \to \Lambda^0 J/\psi$ signals, which is the first cross check for the present analysis. Appendix-A 5.1.1 and The talk [31] presented in the B physics group meeting shows a summary of this study,

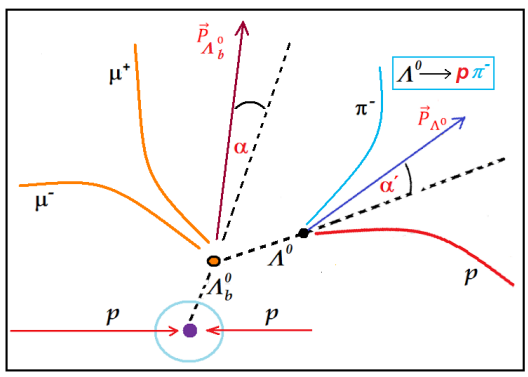

Figure 4–1: $\Lambda_b^0 \to \Lambda^0 \mu^+ \mu^-$ decay topology.

4.2.1 $\mu^+\mu^-$ Selection

For the initial candidates selection, the $\mu^+\mu^-$ pair is selected from muon tracks in the collection, and selected events with two oppositely charged muons with at least one of them reconstructed as a global muon (G) (a muon track that is reconstructed in both tracking and muon system), while the other one can be reconstructed as a tracker (T) (a muon track reconstructed in the tracking system) satisfying the baseline muon looser cuts [32], i.e, the allowed dimuon combination are 2-G and 1G-1T [33].

Additionally, both of these muons must be inside the pseudo-rapidity region where CMS muon reconstruction efficiency is high ($|\eta_\mu| <$2.2), and neither of these muon tracks must be identified with any of the hadron candidates (the pion or the proton) tracks

from the Λ^0 found in the track collection. Furthermore, the muon pair and the Λ^0 are also required to be consistent with originating from a valid common vertex (3 body vertex) with a confidence level (a quantity associated with the χ^2 and this shows a distribution of probability for tracks which are coming from a vertex, is due to the fact that these tracks don't intercept each other)($CL_{vtx}^{\mu^+\mu^-\Lambda^0}$) greater than 1% and reconstructed within the volume of the CMS tracker but significantly displaced from the LHC beam line. We also required that the distance between the muons at their closest approach ($dca_{\mu^+\mu^-}$) be less than 0.5 cm and their crossing point be inside the fiducial tracking volume (Table 4–5).

4.2.2 $\Lambda^0 \rightarrow p\pi^-$ Selection

The default reconstruction sequence in CMSSW includes a step that reconstructs neutral strange hadrons (K_s^0 mesons (($\frac{d\bar{s}-s\bar{d}}{2}$) quark - antiquark state whose mass is 497.61 $\pm$ 0.02 GeV/c^2) and Λ^0, collectively known as V0 particles) using oppositely charged track pairs. Once the $\mu^+\mu^-$ candidate sample has been selected, a selection of Λ^0 baryons is proceded, where they are reconstructed via their decay into a proton and a pion ($\Lambda^0 \rightarrow p\pi^-$) with opposite charge and where the hadron track with the highest p_T is identified as a proton, otherwise identified as a pion. These hadrons also originated from a common vertex, which is required to be displaced from the primary interaction.

The number of reconstructed $\Lambda^0 \rightarrow p\pi^-$ (Fig. 4–2-left) (size of the collection) per event in our MuOnia dataset input shows the number of Λ^0 candidates per event (multiplicity) from where we extracted the Λ_b^0 candidate sample. Due to the fact that the Λ^0 coming from Λ_b^0 are low momentum, the Λ^0 multiplicity has been enhanced with respect to the default vee collection since we have produced it with looser cuts on the Λ^0 two-dimensional (2-dim) vertex and impact parameter significance, where the significance is defined as the ratio of the impact parameter with respect to its uncertainty.

A loose cut of 5.0 (instead of the default value of 15) have been required for the 2-dim vertex significance (*"vtxSignificance2DCut"*) which is defined as the reconstructed $\mathbf{\Lambda^0}$-primary vertex distance in the transverse plane ($\boldsymbol{L_{xy}}$) divided by its standard deviation ($(\boldsymbol{L/\sigma})_{\boldsymbol{xy}}$). A loose cut of 0.5 (instead of 2) was also required for the impact parameter significance (*"impactParameterSigCut"*) defined as the ratio between the perpendicular distance (Ip) from the primary to the initial line of motion of the $\mathbf{\Lambda^0}$ and its standard deviation ($\boldsymbol{Ip/\sigma_{Ip}}$). Table 4–3 shows a summary of these cuts as well as the default collection values. In addition, we required to have valid kinematic vertex fit and $\mathbf{\Lambda^0}$ mass constraint fit to its nominal $\mathbf{\Lambda^0}$ mass [28] in order to consider the $\mathbf{\Lambda^0}$ a good candidate to then combine it with the muon pair.

A gaussian signal plus a linear polynomial fit employed on the p$\boldsymbol{\pi^-}$ invariant mass (Fig. 4–2-right) shows that the "loose" $\mathbf{\Lambda^0}$ candidate sample consists of approximately 24.3$\times\mathbf{10^6}$ $\boldsymbol{\Lambda^0 \rightarrow p\pi^-}$ decays.

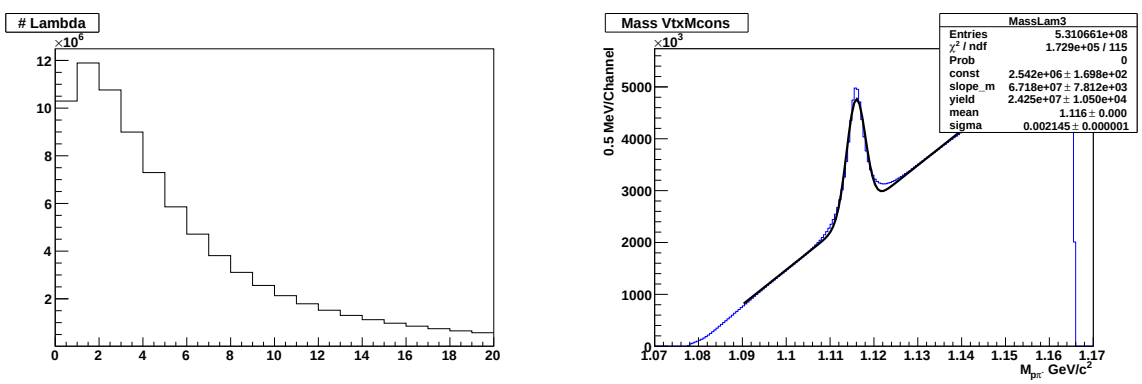

Figure 4–2: $\boldsymbol{\Lambda^0 \rightarrow p\pi^-}$ multiplicity (left) and mass (right).

Table 4–3: Loose $\boldsymbol{\Lambda^0 \rightarrow p\pi^-}$ Selection Cuts

Variable	Applied Cut	Default Cut
$(\boldsymbol{L/\sigma})_{\boldsymbol{xy}}$	>5.0	>15
$\boldsymbol{Ip/\sigma_{Ip}}$	>0.5	> 2

In order to suppress backgrounds from other heavier baryon decays ($\Xi^0 \rightarrow \Lambda^0\pi^0$, $\Sigma^0 \rightarrow \Lambda^0\gamma$, etc.) and to make sure the Λ^0 comes from the $\mu^+\mu^-$ vertex as expected, we required that the cosine of the pointing angle (α) between the Λ^0 and the $\mu^+\mu^-$-Λ^0 vertex direction (see Fig. 4–1) be above 0.9:

$$\cos\alpha_{\Lambda^0-\mu^+\mu^-} = \frac{(\vec{V}_{\mu^+\mu^-} - \vec{V}_{\Lambda^0}) \cdot \vec{P}_{\Lambda^0}}{|\vec{V}_{\mu^+\mu^-} - \vec{V}_{\Lambda^0}||\vec{P}_{\Lambda^0}|} > 0.9$$

in such a way that it points to the 3 body (Λ^0 $\mu^+\mu^-$) vertex position, in comparison with from previous analysis [34] where Λ^0-$\mu^+\mu^-$ vertex was approximated by the $\mu^+\mu^-$ vertex coordinates using a tighter 3-dim cosine Λ^0-$\mu^+\mu^-$ cut.

4.2.3 Λ_b^0 Reconstruction

At this stage, with the help of the topology (Fig. 4–1) and kinematics of the Λ_b^0 particle decays we can determine additional requirements to reconstruct it. In fact, the reconstructed decay length (L) and the Λ_b^0 trajectory pointing to the primary vertex ($\cos\alpha$) are two important variables which help in reducing unwanted prompt dimuon events. In order to select the best primary vertex for this topology, we have searched in the "offlinePrimaryVertices" vertex collection the closest one to the Λ_b^0 trajectory which is calculated by requiring that the cosine in the transverse plane of the angle between the $\mu^+\mu^-$ Λ^0 total momentum ($\vec{P}_{\Lambda_b^0}$) and the primary:

$$\cos\alpha_{prim-\mu^+\mu^-\Lambda^0} = \frac{(\vec{V}_{\mu^+\mu^-\Lambda^0} - \vec{V}_{primary}) \cdot \vec{P}_{\Lambda_b^0}}{|\vec{V}_{\mu^+\mu^-\Lambda^0} - \vec{V}_{primary}||\vec{P}_{\Lambda_b^0}|} > 0.9.$$

The selected primary has been refitted, excluding all the used tracks in the search, the two muons, the proton and the pion, in case the track candidates belong to it.

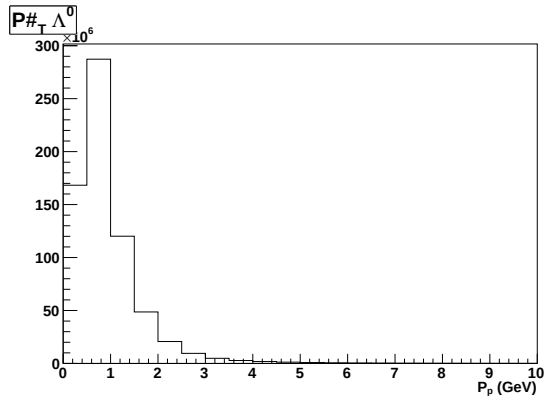

Figure 4–3: Proton Transverse momentum

To calculate the Λ_b^0 ("the Λ^0-$\mu^+\mu^-$ ") vertex detachment distance from the primary vertex, we calculate the decay length (L) in the transverse plane and its uncertainty and then required a minimun detachment by taking the decay length significance ($(L/\sigma)_{\Lambda_b^0}$) greater than 3 (Table 4–5). To clean even further the $\Lambda_b^0 \rightarrow \Lambda^0\mu^+\mu^-$ candidates sample, additional cuts have been applied to purify the Λ^0 (Table 4–4) and the $\mu^+\mu^-$ (Table 4–5) sample.

Table 4–4: $\Lambda^0 \rightarrow p\pi^-$ Selection Cuts

Variable	Applied Cut
$CL_{vtx}^{\Lambda^0\rightarrow p\pi^-}$	>1%
$CL_{massC}^{\Lambda^0}$	>1%
$\lvert M_{p\pi^-} - M_{\Lambda^0}\rvert$	<8 MeV
p_t^p	>1.0 GeV
N_{hits}^p	>6 hits
$N_{hits}^{\pi^-}$	>6 hits
$\lvert M_{K^0_{short}} - M_{\pi^+\pi^-}\rvert$	>20 MeV/c^2

We selected Λ^0 with quality cuts on the vertex confidence level (CL) for pπ^- ($CL_{vtx}^{\Lambda^0\rightarrow p\pi^-}$), on the Λ^0 mass constraint fit ($CL_{massC}^{\Lambda^0}$) and on the reconstructed pπ^- invariant mass, which is required to be 8 MeV around the nominal Λ^0 mass. In addition, to clean even further we requested that the p and π have a minimun number of

Table 4–5: $\mu^+\mu^-$ Selection and Λ_b^0 Reconstruction Cuts

Variable	Applied Cut
$dca_{\mu^+\mu^-}$	<0.5 cm
$CL_{vtx}^{\mu^+\mu^-}$	>1%
both η_μ	<2.2
$(L/\sigma)_{\Lambda^0-\mu^+\mu^-}$	>3
(2D) $\cos\alpha_{\Lambda^0-\mu^+\mu^-}$	>0.9
(2D) $(L/\sigma)_{\Lambda_b^0}$	>3
(2D) $\cos\alpha_{prim-\mu^+\mu^-\Lambda^0}$	>0.9
$CL_{vtx}^{\mu^+\mu^-\Lambda^0}$	>1%

tracking hits (6) and a minimum p_T for the proton (Fig. 4–3) from the Λ^0 of 1.0 GeV to avoid proton mis-identification and to remove undesirable $K_{short}^0 \to \pi^+\pi^-$ cross-feed contamination.

K_{short}^0 Contamination

K_{short}^0 mesons come from decays such as $B^0 \to J/\psi K_{short}^0$ or $B^0 \to \psi(2s)K_{short}^0$ decays (Fig. 4–4) and are included in the input datasets and need to be removed from the sample. To do so, the 2-body (pπ) invariant mass was re-calculated by changing the proton mass assignment for a pion and request that the $\pi^+\pi^-$ invariant mass be smaller than 20 MeV/c^2 around the nominal K_{short}^0 mass [28] to be tag as a K_{short}^0 and then rejected from this analysis. Fig. 4–5 shows the $K_{short}^0 \to \pi^+\pi^-$ contamination ($|M_{K_{short}^0} - M_{\pi^+\pi^-}|$<20 MeV/c^2) in the J/$\psi$ (left side in the upper plot) and in the $\psi(2S)$ (left side in the bottom plot) modes which has been removed (red part) from the Λ_b^0 candidate sample while the right side shows the $\Lambda^0 \to p\pi^-$ kept for the Λ_b^0 sample. Fig. 4–6 shows the remaining negligible B^0 candidates underneath the final Λ_b^0 samples peak.

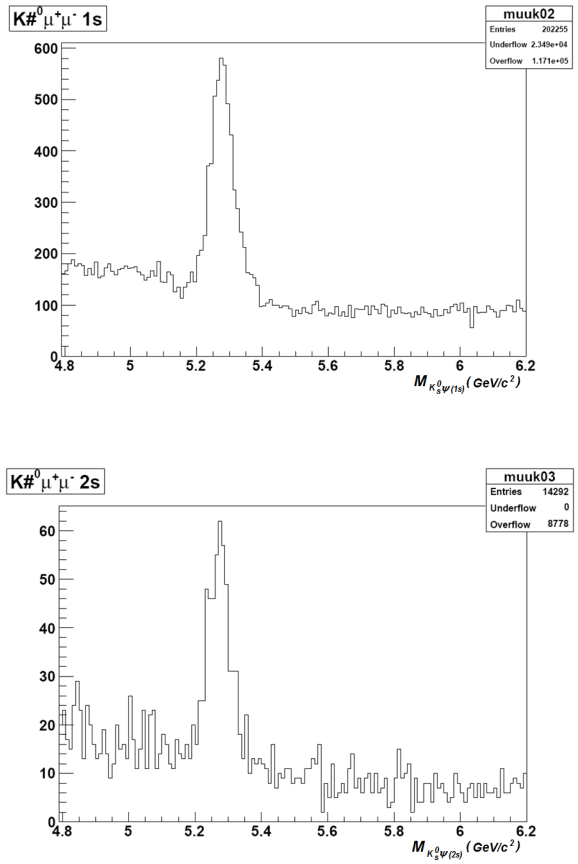

Figure 4–4: Reconstructed invariant mass: K^0_{short} J/ψ (left) and K^0_{short} $\psi(2S)$ (right) in our dataset. A clear B^0 signal is observed which is removed after the Λ^0_b cuts are applied.

This contamination (B^0) is not included in the Λ^0_b MC sample we are using. To make sure that this background is negligible, we have searched for Λ^0_b decay in an enriched B^0 MC dataset [†] . In this sample we have applied all the Λ^0_b base line cuts (Table 4–5, and good pπ^- vertex) but the Λ^0 quality cuts (Table 4–4). The reconstructed $B^0 \to J/\psi K^0_{short}$ and $B^0 \to \psi(2s) K^0_{short}$ are shown in Fig. 4–7. Next we added all the Λ^0 cuts, including the K^0_{short} veto, we obtained that this cross-feed is negligible, despite Λ^0_b and B^0 have a similar topology (Fig. 4–8).

[†] /B0ToPsiMuMu_2MuPEtaFilter_Tight_7TeV-pythia6-evtgen/Fall11-HLTBPh2011_START42_V14B-v2/GEN-SIM-RECO

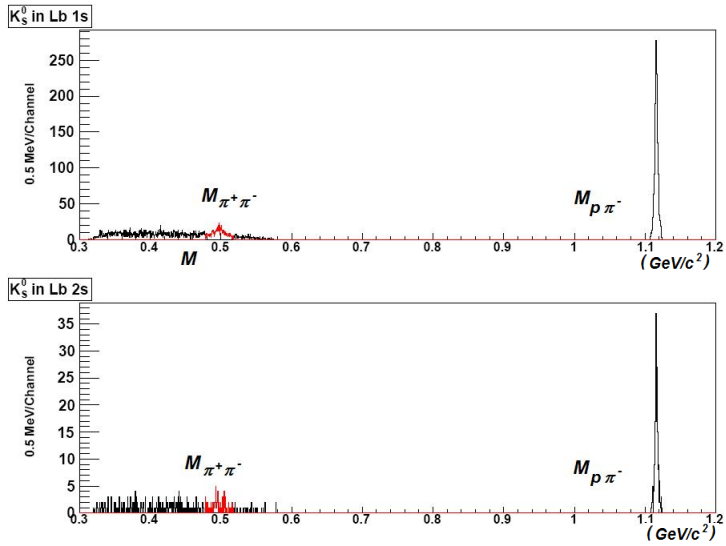

Figure 4–5: pπ^- (graphics right side) and $\pi^+\pi^-$ (graphics left side) invariant masses for the Λ^0 J/ψ sample (top) and Λ^0 $\psi(2S)$ sample (bottom). The Λ^0 on the right is kept while the K^0_{short} contamination ($|M_{K^0_{short}} - M_{\pi^+\pi^-}|$<20 MeV/c^2) is removed in the final Λ^0_b sample.

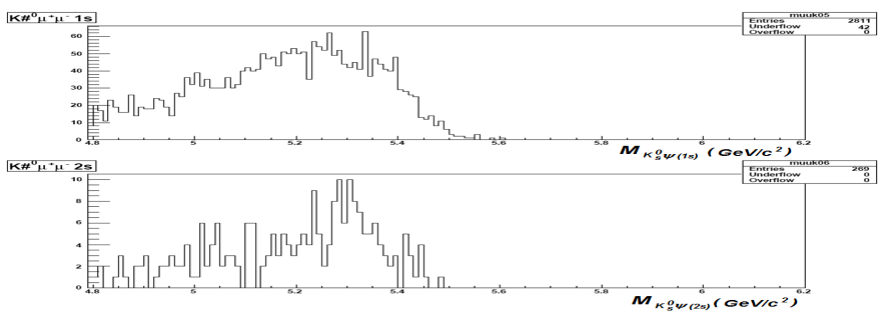

Figure 4–6: B^0 signal (from the data) under the Λ^0_b candidate

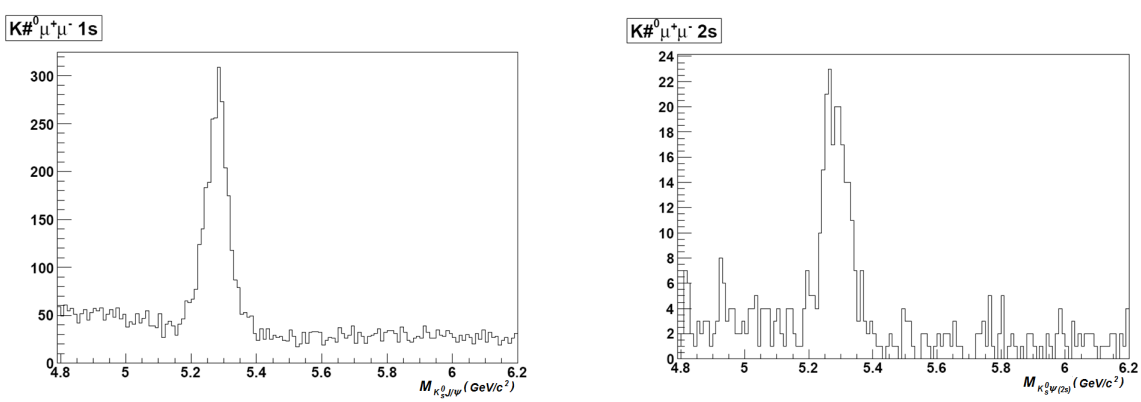

Figure 4–7: Invariant mass for K^0_{short} J/ψ (left) and K^0_{short} $\psi(2S)$ (right). A clear B^0 signal is observed in the MC sample.

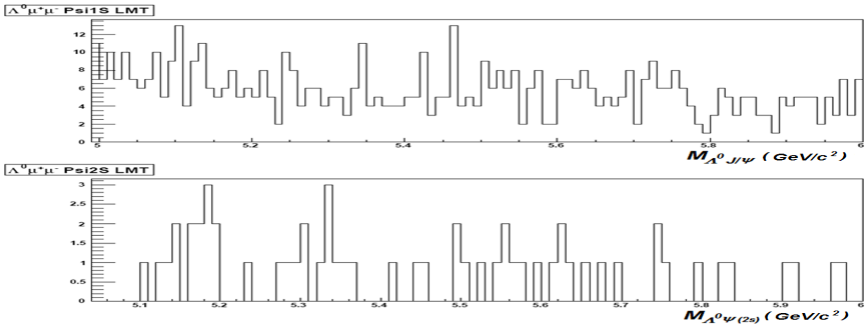

Figure 4–8: Invariant mass for Λ^0 J/ψ (top) and Λ^0 $\psi(2S)$ (bottom). There is not Λ_b^0 signal in the B^0 MC sample, the crossfeed is negligible.

Λ^0 $\mu^+\mu^-$ Data Sample

In order to reduce background in the Λ^0 $\mu^+\mu^-$ sample, we have applied the K^0_{short} veto, vertex confidence levels, the separation significance ($(L/\sigma)_{\Lambda^0-\mu^+\mu^-,2D}$) between Λ^0 and $\mu^+\mu^-$ be greater than 3 to make sure they are coming from 2 well separated vertices, etc. A summary of these cuts are shown in Table 4–4 for Λ^0 and Table 4–5 for the $\mu^+\mu^-$ selection cuts as well as the cuts to select Λ_b^0 candidates (lower part in Table 4–5). Adding all the cuts described in Tables 4–4 and 4–5, we obtain a clear Λ_b^0 peak at its nominal mass of 5.620 GeV/c^2 [28]. Fig. 4–9 shows the Λ^0 $\mu^+\mu^-$ invariant mass, which is the sample from where we look for associate production of $\mu^+\mu^-$ together with Λ^0 particles.

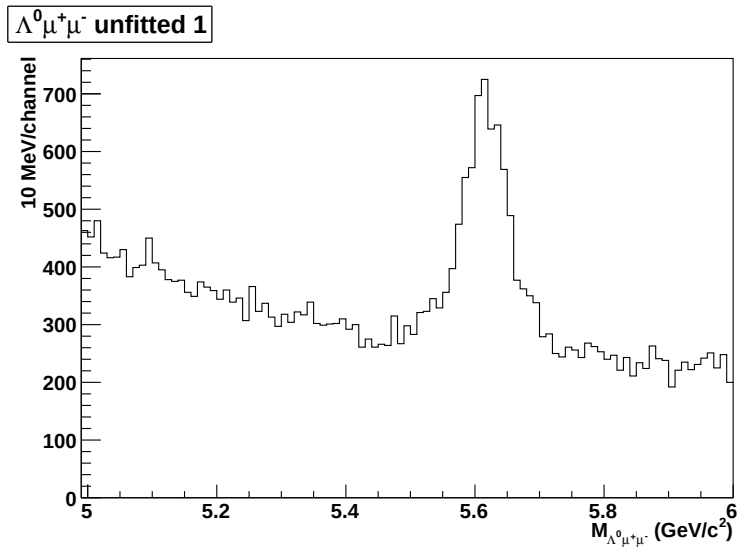

Figure 4–9: $\boldsymbol{\Lambda^0\ \mu^+\mu^-}$ Invariant mass for the 2011 dataset

4.3 $\psi(2S) \rightarrow \mu^+\mu^-$ Data Analysis

We began the study of the $\boldsymbol{\Lambda_b^0 \rightarrow \Lambda^0\psi(2S)}$ decay by investigating the underlying dimuon invariant mass distribution in the $\boldsymbol{\Lambda_b^0 \rightarrow \Lambda^0\mu^+\mu^-}$ candidate sample (Fig. 4–9). Also, we just look the dimuon mass distribution under the $\boldsymbol{\Lambda_b^0}$ baryon resonance (5.620 GeV/c$^{\mathbf{2}}$ $\pm$ 0.05 GeV/c$^{\mathbf{2}}$) shown in Fig. 4–10 where the J/$\boldsymbol{\psi}$ and $\boldsymbol{\psi(2S)}$ mesons decaying into $\boldsymbol{\mu^+\mu^-}$ are clearly reconstructed and constitutes a clear evidence that $\boldsymbol{\Lambda_b^0}$ decays into $\boldsymbol{\Lambda^0}$ J/$\boldsymbol{\psi}$ and also decays into $\boldsymbol{\Lambda^0\ \psi(2S)}$ as well.

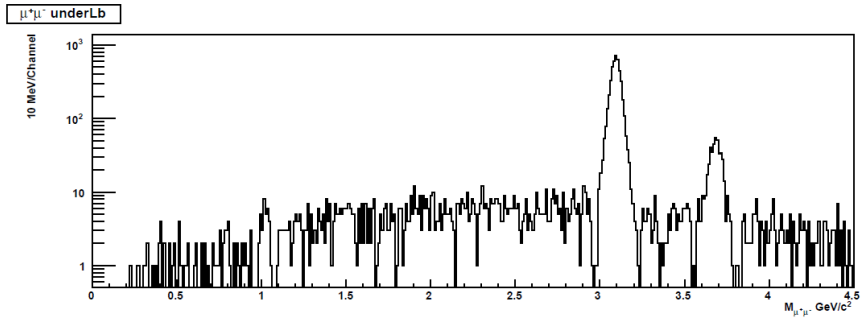

Figure 4–10: $\boldsymbol{M_{\mu^+\mu^-}}$ Invariant Mass.

Next, standard techniques for known $\mu^+\mu^-$ resonances is to apply the mass constrained fit to the measured $\mu^+\mu^-$ system to improve the dimuon momentum resolution and consequently the Λ_b^0 mass resolution. We fitted the dimuon at the 3 body vertex position by constraining the measured $\mu^+\mu^-$ invariant mass to the nominal J/ψ ($\psi(2S)$) mass [28] if the reconstructed $M_{\mu^+\mu^-}$ fell within 150 MeV around the J/ψ ($\psi(2S)$) peak. The confidence level of the mass constraint fit (CL_{massC}) is required to be better than 1%, otherwise the $\mu^+\mu^-$ combination is rejected. Fig. 4–11 shows the candidate sample of $\Lambda_b^0 \to \Lambda^0\psi(2S)$ and $\Lambda_b^0 \to \Lambda^0 J/\psi$ decays after the Λ_b^0 mass resolution has been improved (compared with Fig. 4–9) by the mass constraints fit. Additionaly, kine-

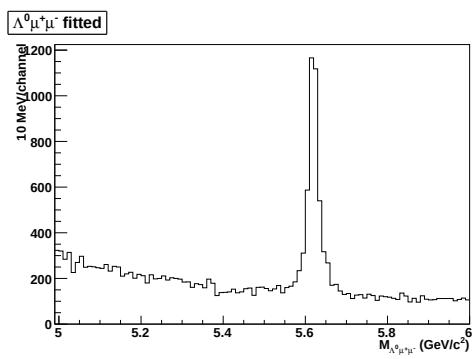

Figure 4–11: Λ^0 $\mu^+\mu^-$ invariant mass for fitted $\mu^+\mu^-$ as J/ψ or $\psi(2S)$

matic cuts (Fig. 4–12) on the Λ_b^0 transverse momentum ($p_t(\Lambda_b^0)$ >10 GeV) and rapidity ($|y(\Lambda_b^0)|$ <2) are then applied in order to reduce remaining combinatorial background (Table 4–7) in our candidate sample.

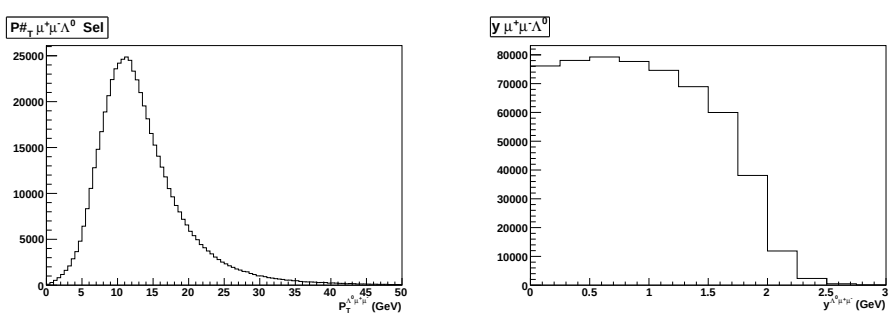

Figure 4–12: Λ^0 $\mu^+\mu^-$ Transverse momentum (left) and Rapidity (right).

4.3.1 $\Lambda_b^0 \to \Lambda^0\psi(2S)$ with $\psi(2S) \to \mu^+\mu^-$

The event topology of these decays (Fig. 4–13) are very similar with the one sketched in Fig. 4–1 with the only difference that in this case the $\mu^+\mu^-$ comes from one of the charmonium states, either J/ψ or $\psi(2S)$.

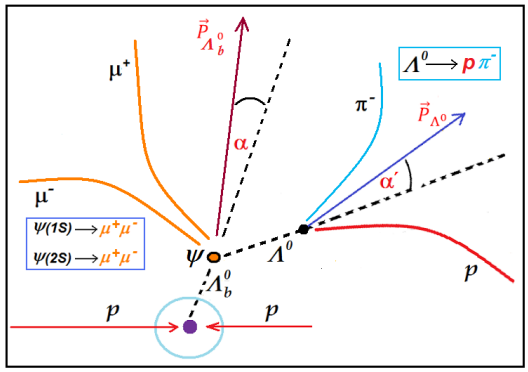

Figure 4–13: $\Lambda_b^0 \to \Lambda^0 J/\psi$ or $\Lambda_b^0 \to \Lambda^0\psi(2S)$ decay topology.

Two more aspects on these decays need to be taken into account before extracting the final $\Lambda_b^0 \to \Lambda^0\psi(2S)$ sample and calculating the total reconstruction efficiency: the trigger used to collect the data (Table 4–1) and the luminosity taken in each of the trigger path.

Displaced Low Dimuon Mass HLT

Because the recorded $\psi(2S)$ event sample in the $\mu^+\mu^-$ decay mode satisfied the Low Mass Trigger (LMT), we required that the normalization J/ψ mode also satisfy the same trigger in order to cancel out the systematic effects. To reduce the HLT low dimuon mass trigger rate, it was taken with a variable muon p_T, dimuon vertex confidence level (CL) and p_T threshold (Table 4–6) as the instantaneous luminosity increased [29]. Table 4–6 shows in addition, the total L for each of the trigger path used in this analysis as well as the fraction with respect to the total L (5.0 fb^{-1}).

In this analysis, we have applied all these cuts and a transverse $\mu^+\mu^-$ momentum cut

Table 4–6: Displaced Low Dimuon Mass Trigger (LMT)

HLT	Trigger Path	L	p_T	CL	Fraction
		(pb^{-1})	(GeV)	(%)	(%)
0	HLT_Dimuon6p5_LowMass_Displaced_v*	174.8			3.49
1	HLT_Dimuon7_LowMass_Displaced_v*	984.0	3.0	5	19.66
2	HLT_DoubleMu4_LowMass_Displaced_v*	884.4	4.0	15	17.67
3	HLT_DoubleMu4p5_LowMass_Displaced_v*	2738.4	4.5	15	54.71
4	HLT_DoubleMu5_LowMass_Displaced_v*	398.7	5.0	15	7.97

of 6.9 GeV in order to match the LMT conditions since the other requirements for the trigger (Table 4–5) were already applied. Table 4–7 summarized the additional cuts to extract these exclusive decays as well as to match the LMT.

Table 4–7: Kinematics cuts and LMT matching offline cuts

Variable	Applied Cut
$\lvert M_{J/\psi} - M_{\mu^+\mu^-}\rvert$	<150 MeV
$\lvert M_{\psi(2S)} - M_{\mu^+\mu^-}\rvert$	<150 MeV
CL_{massC}	>1%
$p_t(\Lambda_b^0)$	>10 GeV
$\lvert y(\Lambda_b^0)\rvert$	<2
$P_T\ \mu^+\mu^-$	>6.9 GeV

MC Trigger Relative Efficiency

In order to extract the relative efficiency, we have splitted the MC final signal sample ($\Lambda_b^0 \rightarrow \Lambda^0 J/\psi$ and $\Lambda_b^0 \rightarrow \Lambda^0 \psi(2S)$ candidates) by trigger paths (Fig. 4–14) to then weight them by the corresponding trigger fraction (Table 4–6). The HLT0 path (top Fig. 4–14), which corresponds to the /MuOnia/Run2011A-May10ReReco-v1/AOD, doesn't contain any valid data for this analysis.

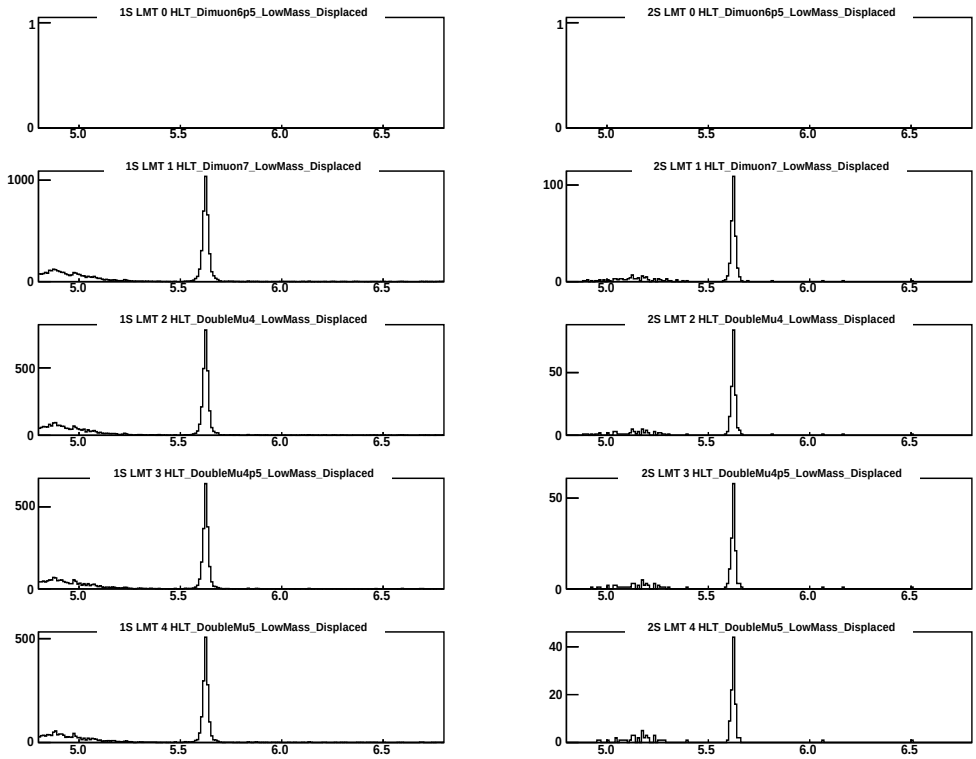

Figure 4–14: MC $\Lambda_b^0 \to \Lambda^0 J/\psi$ (left) and $\Lambda_b^0 \to \Lambda^0 \psi(2S)$ (right) signal by trigger path.

Because there is no background on these Λ_b^0 signal MC, we have just counted the number of events in the peak (with no statistical error) and weigthed them by the LMT fraction to calculate the relative efficiency.

$$f_{rec}^{MC} = \frac{(N_{HLT1} + N_{HLT2} + N_{HLT3} + N_{HLT4})^{\Lambda_b^0 \to \Lambda^0 J/\psi}}{(N_{HLT1} + N_{HLT2} + N_{HLT3} + N_{HLT4})^{\Lambda_b^0 \to \Lambda^0 \psi(2S)}}.$$

where N_{HLT1} is the reconstructed MC Λ_b^0 yield weighted by the trigger fraction path number 1 (last column on Table 4–6), N_{HLT2} for the trigger path number 2, etc. The actual MC data from these distribution give us:

$$\frac{3332 \times 19.6\% + 2361 \times 17.6\% + 1840 \times 54.7\% + 1420 \times 7.9\%}{267 \times 19.6\%\% + 185 \times 17.6\% + 129 \times 54.7\% + 96 \times 7.9\%} = 13.42.$$

Note that the corresponding calculation does not include correction in p_T and η for the acceptance.

Final Λ_b^0 Candidate Sample

Finally, we computed the Λ_b^0 invariant mass by combining the Λ^0 and $\mu^+\mu^-$ four-momentum, where both of them were fitted with mass constraints at their common vertex. Then the Λ_b^0 sample , including the LMT, the invariant mass of the Λ^0 and $\psi(2s)$ candidates were fitted using a sum of two gaussian function with the same mean each to describe the signal peak and a second degree Chevycheb Polynomial function for the background (Fig. 4–15).

At the same time, to calculate the relative Λ_b^0 reconstruction efficiency, we analyzed the MC sample and treated it under the same conditions as data, including the HLT. The number of signal (S) events obtained in the fit for data and for the Λ_b^0 Monte Carlo signal is reported in Table 4–8 (and in Fig. 4–15).

The widths for the $\psi(2s)$ mode in data fit were adjusted with the ones used in the MC $\psi(2s)$ mode. The fitted mass for the $\Lambda_b^0 \rightarrow \Lambda^0\psi(2S)$ is 5.623 $\pm$0.003 GeV. As this signal is large enough, the significance is estimated by $S/\sqrt{S+B}$, which in this case is 12.5σ.

Table 4–8: Number of Events in the $\psi(2S) \rightarrow \mu^+\mu^-$ Mode (displaced low dimuon mass trigger (LMT))

Decay Mode	S (Events)	Signif	$S_{MC}(Events)$
$\Lambda_b^0 \rightarrow \Lambda^0\psi(2S)$	203.55 $\pm$16.25	12.5σ	263.842 $\pm$16.39
$\Lambda_b^0 \rightarrow \Lambda^0 J/\psi$	2115.40 $\pm$63.66	36.8σ	3392.71 $\pm$59.00

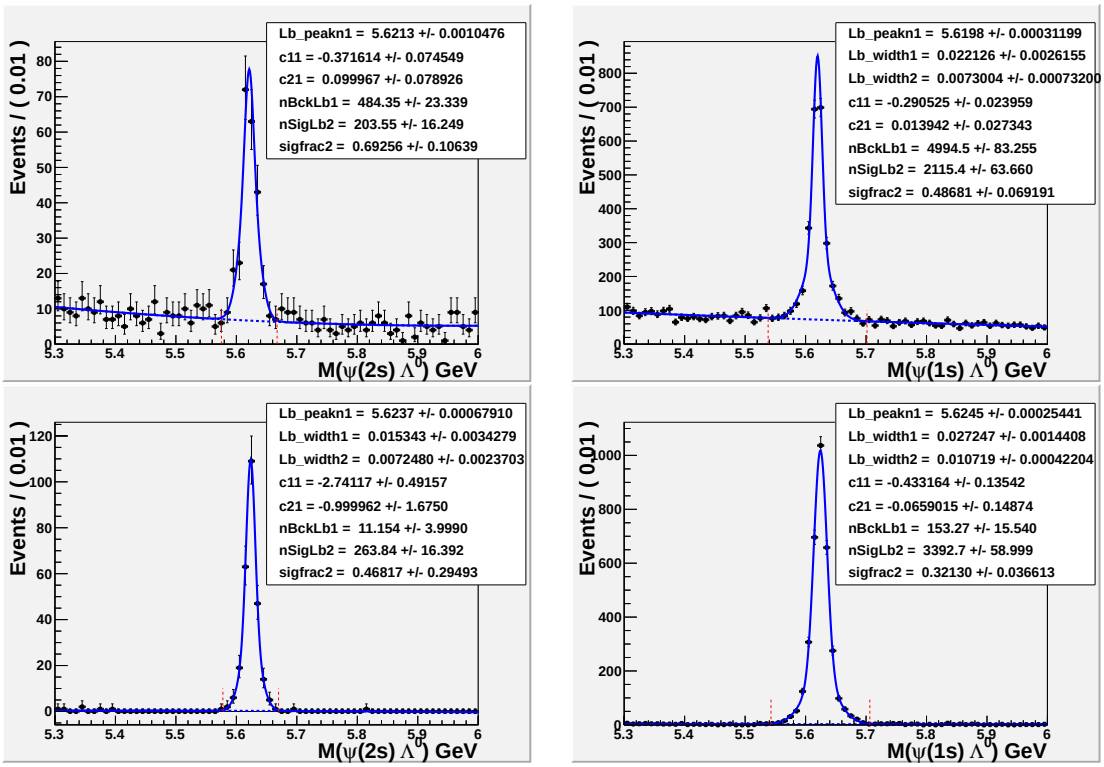

Figure 4–15: Λ^0 $\psi(2S)$ (left) and Λ^0 J/ψ (right) Mass. Top(data) and Bottom(mc).

4.4 $\psi(2S) \to J/\psi\pi^+\pi^-$ Data Analysis

Because the $\psi(2S)$ branching fraction decaying into a dimuon ($\mu^+\mu^-$) is very small (B($\psi(2S) \to \mu^+\mu^-$)=0.77%) [28], we tried to search the process $\psi(2S) \to$ J/$\psi\pi^+\pi^-$, where it is known to be the largest decay mode of the $\psi(2S)$.

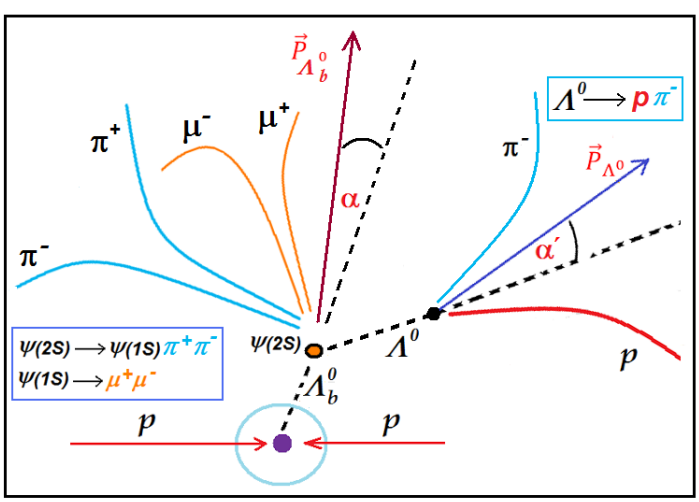

Figure 4–16: $\Lambda_b^0 \to \Lambda^0\psi(2S)$ decay topology with $\psi(2S) \to J/\psi\pi^+\pi^-$.

The branching fraction B($\psi(2S) \to J/\psi\pi^+\pi^-$) $\sim$2% gives a bigger contribution than the previous 0.77%, which represents an increase of a factor of $\sim$2.6 with respect to the $\mu^+\mu^-$ channel, assuming 100% reconstruction efficiency for $\pi^+\pi^-$. The details of the $\Lambda_b^0 \to \Lambda^0\psi(2S)$ analysis in the next section confirm that this decay channel can be observed.

4.4.1 $\Lambda_b^0 \to \Lambda^0\psi(2S)$ with $\psi(2S) \to J/\psi\pi^+\pi^-$

The event topology (Fig. 4–16) in this search is very similar to the previous Λ_b^0 decay mode but in this case we have two extra hadrons ($\pi^+\pi^-$) attached to the secondary vertex (Λ^0 $\mu^+\mu^-$), which is the $\psi(2S)$ decaying into J/ψ $\pi^+\pi^-$ and $J/\psi \to \mu^+\mu^-$. The Λ^0 and the $\mu^+\mu^-$ selection criteria used in this part of the analysis are basically the same as the one described in section 4.2.2 and 4.2.1 respectively, however, even though the Λ_b^0 reconstruction (section 4.2.3) cuts are conceptually the same as previously used, they are tighter in this case in order to avoid combinatorial background coming from $\pi^+\pi^-$ combinations from the $\psi(2S)$ reconstruction.

$\psi(2S) \to J/\psi\pi^+\pi^-$ Reconstruction

Once the $\Lambda^0 \to p\pi^-$ (all cuts on Table 4–4, including Λ^0 mass fit, K^0_{short} rejection, etc.) and the $\mu^+\mu^-$ (all cuts on [32] and on the top part of Table 4–5) are selected, we ran the search program in a wide dimuon region (2.8 $< M_{\mu^+\mu^-} <$4.0 GeV) to include background events for further studies and to search for $\pi^+\pi^-$ that combined with the $\mu^+\mu^-$, coming from J/ψ, which come from a common vertex, will form the $\psi(2S) \to J/\psi\pi^+\pi^-$ decay. We selected $\pi^+\pi^-$ by choosing 2 oppositely charged tracks, reconstructed in the *"cleanPatTrackCands"* tracks collection, distinct from the used $\mu^+\mu^-$ and pπ^- reconstructed tracks.

As an approach to reduce the number of $\pi^+\pi^-$ candidates in this high track multiplicity environment, we have considered only $\pi^+\pi^-$ pairs with a minimum transverse momentum ($p_t^{\pi^+\pi^-}$) of 0.75 GeV and p_t^{π}>0.25 GeV for each individual pion. In addition, reconstructed pion and $\mu^+\mu^-$ are required to be close kinematically by considering a geometric bounding in the $\eta\phi$ of the pion track relatice to the muon tracks

$$R_{\mu^+\mu^-\pi} = \sqrt{\left(\eta_{\mu^+\mu^-} - \eta_\pi\right)^2 + \left(\Phi_{\mu^+\mu^-} - \Phi_\pi\right)^2} < 0.75,$$

where $\left(\eta_{\mu^+\mu^-} - \eta_\pi\right)$ and $\left(\Phi_{\mu^+\mu^-} - \Phi_\pi\right)$ are the pseudo-rapidity and azimuthal angle respectively for the $\mu^+\mu^-$ and the charged pion track. Once the number of combinations has been reduced, we requested that the distance closest of approach between these 4 tracks be $<$ 0.5 cm and their crossing point be reconstructed inside the fiducial tracking volume. Then, we calculated the $\mu^+\mu^-$ $\pi^+\pi^-$ vertex and request that the reconstructed CL be greater than 1%.

A summary of these cuts are shown in Table 4–9 and the reconstructed $\mu^+\mu^-$ $\pi^+\pi^-$ mass in Fig. 4–17 show a clear $\psi(2S) \to J/\psi\pi^+\pi^-$ peak at its nominal mass where the $\mu^+\mu^-$ mass has been required to be 150 MeV/c^2 around the J/ψ nominal mass where a confirmation of the $\psi(2S) \to J/\psi\pi^+\pi^-$ reconstruction decay channel can be appreciated.

Table 4–9: $\psi(2S) \to J/\psi\pi^+\pi^-$ Reconstruction Cuts

Variable	Applied Cut
$p_t^{\pi^+\pi^-}$	>0.75 GeV
p_t^{π}	>0.25 GeV
$R_{\mu^+\mu^-\pi}$	<0.75
$CL_{vtx}^{\mu^+\mu^-\pi^+\pi^-}$	>1%
$\lvert M_{J/\psi} - M_{\mu^+\mu^-}\rvert$	<150 MeV

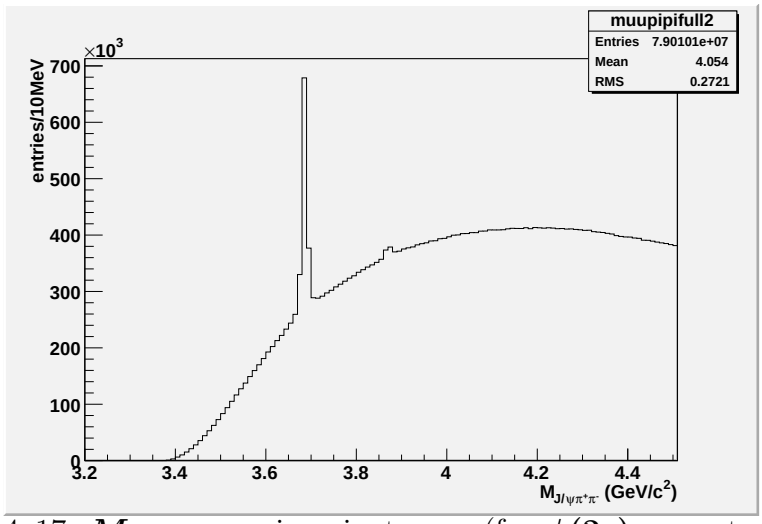

Figure 4–17: $M_{\mu^+\mu^-\pi^+\pi^-}$ invariant mass (for $\psi(2s)$ reconstruction).

Λ_b^0 Reconstruction

As it was discussed earlier (section 4.2.3), and taking advantage of the previous event decay topology (Fig. 4–16) and kinematics of the long lived Λ_b^0 particle decays, we computed the Λ_b^0 ("the Λ^0 $\mu^+\mu^-$ $\pi^+\pi^-$ ") vertex detachment distance from the primary interaction.

The primary vertex was selected in the same way as in the case of $\psi(2S) \rightarrow \mu^+\mu^-$ mode (section 4.2.3) and re-fitting the CMS primary vertex, excluding all the 6 tracks involved in this search, and then required a good quality on the re-fitted primary vertex (confidence level $CL_{primary}$>5%), a minimun detachment ($(L/\sigma)_{\Lambda_b^0,2D} > 3$) and Λ_b^0 pointing trajectory to its production point by requiring the cosine of the angle between $\mu^+\mu^-$ $\pi^+\pi^-$ (which is also the Λ^0 $\mu^+\mu^-$ $\pi^+\pi^-$ vertex) and the primary:

$$\cos\alpha_{prim-\mu^+\mu^-\pi^+\pi^-} = \frac{(\vec{V}_{\mu^+\mu^-\pi^+\pi^-} - \vec{V}_{primary}) \cdot \vec{P}_{\Lambda_b^0}}{|\vec{V}_{\mu^+\mu^-\pi^+\pi^-} - \vec{V}_{primary}||\vec{P}_{\Lambda_b^0}|} > 0.95.$$

as we did in section 4.2.3. Table 4–10 summarized these cuts, HLT displaced Low Mass Trigger was applied. A Λ_b^0 signal can be appreciated as shown in Fig 4–18.

Table 4–10: Λ_b^0 Reconstruction cuts in the $\psi(2S) \to J/\psi\pi^+\pi^-$ mode.

Variable	Applied Cut
$(L/\sigma)_{\Lambda^0-\mu^+\mu^-\pi^+\pi^-}$	>3
$\cos\alpha_{\Lambda^0-\mu^+\mu^-\pi^+\pi^-}$	>0.9
$CL_{primary}$	$>5\%$
$(L/\sigma)_{\Lambda_b^0}$	>3
$\cos\alpha_{prim-\mu^+\mu^-\pi^+\pi^-}$	>0.95

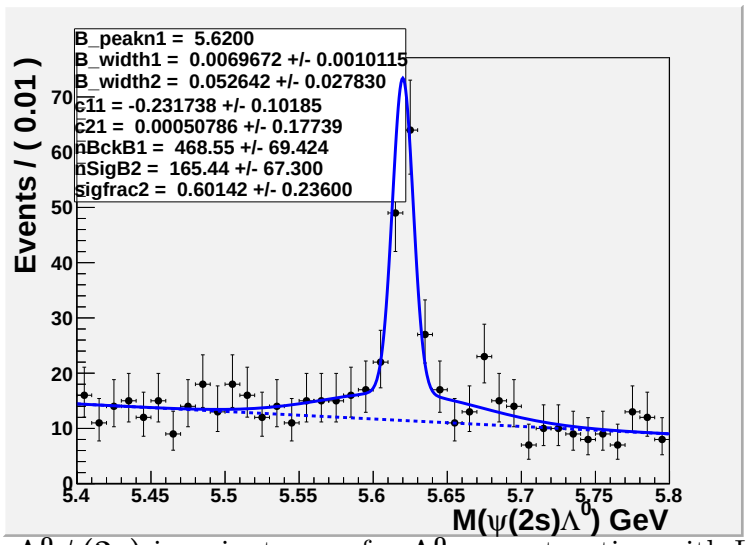

Figure 4–18: $\Lambda^0\psi(2s)$ invariant mass for Λ_b^0 reconstruction with LMT trigger.

4.4.2 Λ_b^0 Branching Ratio Measurements

The absolute branching fraction for a particle decay is given by the fraction of produced particles that later decay in a channel in particular, with respect to the number of decaying particles [17] [35]. For the $\Lambda_b^0 \to \Lambda^0\psi(2S)$, its branching fraction is measured by

$$B(\Lambda_b^0 \to \Lambda^0\psi(2S)) = \frac{N_{\Lambda_b^0\to\Lambda^0\psi(2S)}}{\epsilon^{rec} * \mathscr{L} * B(\psi(2S) \to X) * B(\Lambda^0 \to p\pi^-)}, \qquad (4.1)$$

where it is given in terms of the number of observed $\Lambda_b^0 \to \Lambda^0\psi(2S)$ events in "data" $N_{\Lambda_b^0\to\Lambda^0\psi(2S)}$, $\mathscr{L}$ is the integrated luminosity, B($\Lambda^0 \to p\pi^-$) and B($\psi(2S) \to$X) are

the branching fraction for the Λ^0 and $\psi(2S)$ decay respectively, and ϵ^{rec} is the $\Lambda_b^0 \to \Lambda^0\psi(2S)$ MC total reconstruction efficiency which included all the steps (acceptance, tracks reconstruction, offline cuts, trigger match, etc.) involved in the Λ_b^0 reconstruction. The $\psi(2S)$ final state X represents in this case only $\mu^+\mu^-$ because the decay mode $\psi(2S) \to J/\psi\pi^+\pi^-$ is still in progress. Similarly, the absolute branching fraction for the $\Lambda_b^0 \to \Lambda^0 J/\psi$ is given by:

$$B(\Lambda_b^0 \to \Lambda^0 J/\psi) = \frac{N_{\Lambda_b^0 \to \Lambda^0 J/\psi}}{\epsilon^{rec} * \mathscr{L} * B(J/\psi \to \mu^+\mu^-) * B(\Lambda^0 \to p\pi^-)}, \tag{4.2}$$

where $N_{\Lambda_b^0 \to \Lambda^0 J/\psi}$ is the number of $\Lambda_b^0 \to \Lambda^0 J/\psi$ events reconstructed in data and equivalently (with Eq. (4.1)) the other terms but in this case for $\Lambda_b^0 \to \Lambda^0 J/\psi$.

Taking advantage that both of these modes are very similar and have similar topology, it is very convenient to measure the unknown signal branching fraction B($\Lambda_b^0 \to \Lambda^0\psi(2S)$) with respect to the known B($\Lambda_b^0 \to \Lambda^0 J/\psi$) in such a way that the integrated luminosity and the systematics uncertainties due to reconstruction and trigger cancel out when both samples come from the same dataset input (as this analysis) and both samples satisfied exactly the same trigger.

Thus, dividing equation (4.1) by equation (4.2) and canceling $\mathscr{L}$, and B($\Lambda^0 \to p\pi^-$), the relative branching fraction formula is:

$$\frac{B(\Lambda_b^0 \to \Lambda^0\psi(2S))}{B(\Lambda_b^0 \to \Lambda^0 J/\psi)} = \frac{N_{\Lambda_b^0 \to \Lambda^0\psi(2S)}}{N_{\Lambda_b^0 \to \Lambda^0 J/\psi}} \left(\frac{\epsilon_{\Lambda_b^0 \to \Lambda^0 J/\psi}}{\epsilon_{\Lambda_b^0 \to \Lambda^0\psi(2S)}}\right)^{rec} * f_c, \tag{4.3}$$

where the PDG [28] branching fraction factor is:

$$f_c = \frac{B(J/\psi \to \mu^+\mu^-)}{B(\psi(2S) \to X)},$$

which in the case of $\psi(2S) \to \mu^+\mu^-$, B($\psi(2S) \to$X) $\equiv$ B($\psi(2S) \to \mu^+\mu^-$), f_c is:

$$f_c = \frac{B(J/\psi \to \mu^+\mu^-)}{B(\psi(2S) \to \mu^+\mu^-)} = \frac{5.93\% \pm 0.06\%}{0.77\% \pm 0.08\%} = 7.7013 \pm 0.8039(stat). \tag{4.4}$$

Now, we used the MC sample to measure the relative Λ_b^0 reconstruction efficiency:

$$\left(\frac{\epsilon_{\Lambda_b^0\to\Lambda^0 J/\psi}}{\epsilon_{\Lambda_b^0\to\Lambda^0\psi(2S)}}\right)^{rec} = f_{rec}^{MC} * f_{gen} \tag{4.5}$$

where the generated MC factor is

$$f_{gen} = \left(\frac{N_{\Lambda_b^0\to\Lambda^0\psi(2S)}}{N_{\Lambda_b^0\to\Lambda^0 J/\psi}}\right)^{Gen}$$

and the reconstructed MC factor is defined as

$$f_{rec}^{MC} = \left(\frac{N_{\Lambda_b^0\to\Lambda^0 J/\psi}}{N_{\Lambda_b^0\to\Lambda^0\psi(2S)}}\right)^{MCrec}.$$

The total number of generated events are counted by using the MC generated branching fraction from Table 4–2 which in the case of the $\psi(2S) \to \mu^+\mu^-$ is:

$$f_{gen} = \frac{B_{gen}(\Lambda_b^0 \to \Lambda^0\psi(2S))}{B_{gen}(\Lambda_b^0 \to \Lambda^0 J/\psi)} * \frac{B_{gen}(\psi(2S) \to \mu^+\mu^-)}{BB_{gen}(J/\psi \to \mu^+\mu^-)} = \frac{0.053}{0.168} * \frac{0.1741}{1} = 0.055 \tag{4.6}$$

here we introduce an acceptance correction factor (f_{acc}) to be multiplied with f_{acc} since our MC dataset has been filtered for muons with $p_t > 2.5$ GeV and $|\eta| < 2.5$. In order to calculate f_{acc}, we have generated 50 million events under exactly the same conditions as our MC dataset, obtaining, by matching the truth MC decay sequence, $f_{acc} = (N_{\Lambda_b^0\to\Lambda^0\psi(2S)}/N_{\Lambda_b^0\to\Lambda^0 J/\psi})^{acc} = 1.236$ which implies that the "corrected" generated factor is:

$$f_{gen} = 0.06810 \pm 0.00421$$

where the statistical error (≈6.2%) is due to the limited MC statistics that will be included in the systematic uncertainties (section 4.4.3).

Replacing the relative reconstruction efficiency (eq. (4.5)) in (eq. (4.3)), we obtain the final expression for the relative branching fraction:

$$\frac{B(\Lambda_b^0 \to \Lambda^0\psi(2S))}{B(\Lambda_b^0 \to \Lambda^0 J/\psi)} = \left(\frac{N_{\Lambda_b^0\to\Lambda^0\psi(2S)}}{N_{\Lambda_b^0\to\Lambda^0 J/\psi}}\right) * f_{rec}^{MC} * f_{gen} * f_c. \tag{4.7}$$

Measurement $\mathrm{B}(\Lambda_b^0 \to \Lambda^0\psi(2S))$ with $\psi(2S) \to \mu^+\mu^-$

In order to measure the relative branching fraction, the yields from Table 4–8 are replaced in formula (4.7):

$$\frac{B(\Lambda_b^0 \to \Lambda^0\psi(2S))}{B(\Lambda_b^0 \to \Lambda^0 J/\psi)} = \left[\frac{203.55 \pm 16.25}{2115.40 \pm 63.66}\right] * [13.42] * 0.06810 * (7.7013 \pm 0.8039),$$

where the factors f_{gen} and f_c were taken from equation (4.6) and (4.4) and the relative reconstructed "efficiency" $f_{rec}^{MC}(\Lambda^0\ \mathrm{J}/\psi/\Lambda^0\ \psi(2S))$ was calculated by weighthing the MC trigger path Λ_b^0 signal by the trigger fraction from Table 4–6 [31], as discussed in section 4.3.1.

Calculating, we obtained a preliminary measurement for this mode:

$$\frac{B(\Lambda_b^0 \to \Lambda^0\psi(2S))}{B(\Lambda_b^0 \to \Lambda^0 J/\psi)} = 0.669 \pm 0.057(stat) \pm 0.043(syst) \pm 0.077(PDG)$$

where the last term is the uncertainty from the ratio $\mathrm{B}(\psi(2S) \to \mu^+\mu^-)/\mathrm{B}(J/\psi \to \mu^+\mu^-)$ taken from the PDG [28] and the systematic uncertainties included only the biases due to background shape and MC statistics, and are described in the next section. The analysis to determine the relative branching of $\Lambda_b^0 \to \Lambda^0\psi(2S)$ to $\Lambda_b^0 \to \Lambda^0 J/\psi$ with $\psi(2S) \to J/\psi\pi^+\pi^-$ decay mode is still in progress. Examinations and analysis are being studied to estimate this rate.

4.4.3 $\Lambda_b^0 \to \Lambda^0\psi(2S)$ Systematic Uncertainties

The systematic uncertainties on the branching fraction are based on background parameterization and limited MC statistics (6.18%) since the pile-up (number of primary interactions per bunch [36]) is not significant.

Split Sample by Run Period

A split sample test is an experimental method which a sample is divided into sub-samples that are treated differently. The candidate sample for this analysis consists of two run periods, namely Run 2011-A and 2011-B, with approximately the same integrated luminosity (Table 4–1) but with a different average number of reconstructed primary interactions (pile-up) as shown in Fig. 4–19. In order to study the pile-up dependence

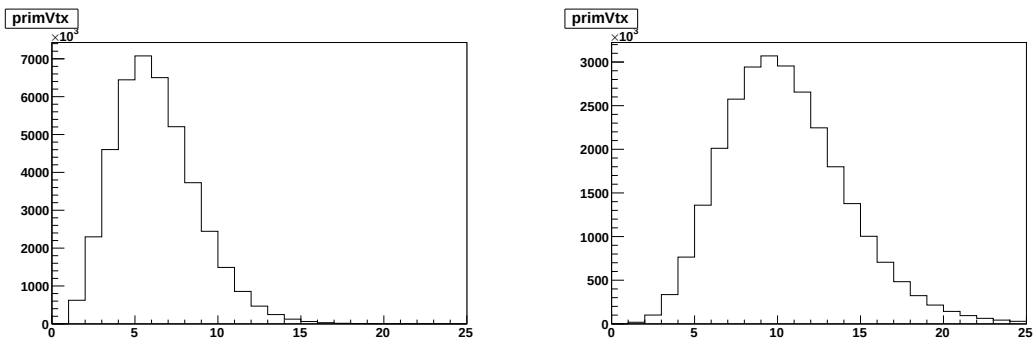

Figure 4–19: Primary Vertexes Multiplicity for Run 2011 A (left) and B (right).

for this analysis, we have measured (see appendix-B 5.1.2) the number of event for each of these signal ($\boldsymbol{\Lambda^0}$ J/$\boldsymbol{\psi}$ and $\boldsymbol{\Lambda^0}$ $\boldsymbol{\psi(2S)}$) on each of the run periods (Table 4–11), concluding that the event ratio remains constant (within the statistical error) and higher pile-up as Run 2011-B did not significantly degraded the event rate. No systematics are yet assigned due to pile-up. We don't expect systematics from this source (this work is in progress).

Table 4–11: Number of Signal Events as a Function of the Dataset. (Sign=S/$\boldsymbol{\sqrt{S+B}}$)

DataSet	$\boldsymbol{\Lambda_b^0 \to \Lambda^0 J/\psi}$	Sign	$\boldsymbol{\Lambda_b^0 \to \Lambda^0 \psi(2S)}$	Sign	$\boldsymbol{\Lambda^0}$ $\boldsymbol{\psi(2S)}$/$\boldsymbol{\Lambda^0}$ J/$\boldsymbol{\psi}$
Run2011-A	1247.15 ±46.76	28.2	125.51 ±12.82	10.0	0.100 ±0.011
Run2011-B	862.01 ±41.31	23.6	74.34 ±10.25	7.6	0.086 ±0.013

A summary of the source of systematic uncertainties are listed in table 4–12. These were combined (Total) using a root sum-of-the-squares approach (in quadrature) to give an

estimate for the total relative uncertainty on the branching fraction.

Table 4–12: Systematic Uncertainties

Source	Cut Value	Variation wrt the central value
Background shape	2Gauss + P3 (Chevycheb)	+1.49%
Limited MC Statistics	Statistics error on $\epsilon_{1s}/\epsilon_{2s}$	+6.18%
Total		6.36%

The total systematic uncertainty is 6.36%, with no significant deviation from the central value.

This analysis has been cross checked (in our group) by an independent analysis [34] looking for dimuon first to then looking for Λ^0 as oppossed to the present work where we started "looping" in the other way around. No difference in the final result was found and no systematics is assigned due to the Λ_b^0 search method.

CHAPTER 5
CONCLUSIONS

The preliminary relative branching fraction B($\Lambda_b^0 \rightarrow \Lambda^0\psi(2S)$)/B($\Lambda_b^0 \rightarrow \Lambda^0 J/\psi$) using LMT with $\psi(2S) \rightarrow \mu^+\mu^-$ was measured to be:

$$\frac{B(\Lambda_b^0 \rightarrow \Lambda^0\psi(2S))}{B(\Lambda_b^0 \rightarrow \Lambda^0 J/\psi)} = 0.669 \pm 0.057(stat) \pm 0.043(syst) \pm 0.077(PDG).$$

This observation and measurement on the Λ_b^0 baryon is the first one of this kind and follows the same trends as many other B meson branching fraction decaying into charmonium final states, as for instance [28];

$$\frac{B(B^+ \rightarrow K^+\psi(2S))}{B(B^+ \rightarrow K^+ J/\psi)} = 0.65 \pm 0.05$$

Fig. 5–1 shows these relative branching fraction decaying into charmonium states ($\psi(2S)$ +X)/(J/ψ +X) where X represents a π^+, K^0_{short}, Λ^0, etc.

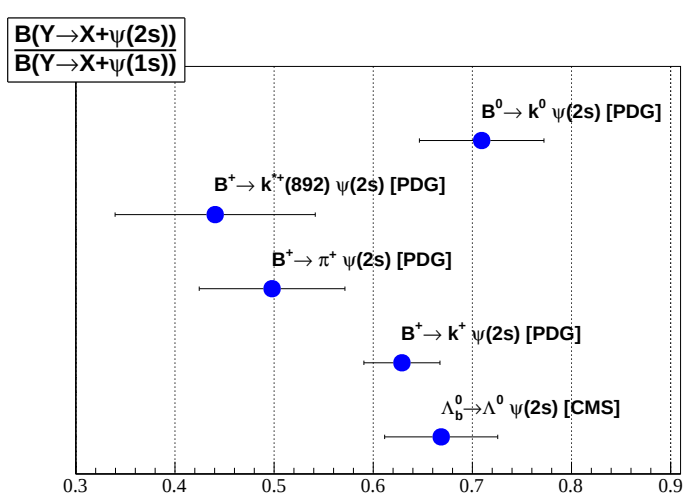

Figure 5–1: Relative branching fraction for b baryons (CMS) and meson (PDG).

We were able to independently confirm our observation of the $\Lambda_b^0 \rightarrow \Lambda^0\psi(2S)$ decay using one of the $\psi(2S)$ "golden" mode decays ($\psi(2S) \rightarrow J/\psi\pi^+\pi^-$). The data analysis of $\Lambda_b^0 \rightarrow \Lambda^0\psi(2S)$ with the $\psi(2S) \rightarrow J/\psi\pi^+\pi^-$ decay mode shows a preliminar signal of 165 events.

5.0.4 Future works

Those are preliminary results. However, this analysis is still in progress. As future works for the present analysis, for $\Lambda_b^0 \rightarrow \Lambda^0\psi(2S)$ decay we have the following:

- Analysis in $\Lambda_b^0 \rightarrow \Lambda^0\psi(2S)$ MC sample.

- Analysis in $\Lambda_b^0 \rightarrow \Lambda^0\psi(2S)$ MC sample.

- Selection cuts for isolation of pion tracks in the $\psi(2S) \rightarrow J/\psi\pi^+\pi^-$ mode.

- Adjustment for $\Lambda^0\psi(2s)$ mass fit in $\Lambda_b^0 \rightarrow \Lambda^0\psi(2S)$ reconstruction.

- Extra cuts have to be taken for appropiate calculations for the relative fraction of B($\Lambda_b^0 \rightarrow \Lambda^0\psi(2S)$) to B($\Lambda_b^0 \rightarrow \Lambda^0 J/\psi$).

5.1 Appendix

5.1.1 Appendix A: Λ_b^0 Cross Section Analysis for 2011-A

The reproduction of the main distributions ($\Lambda_b^0 \rightarrow \Lambda^0 J/\psi$, J/$\psi$ and Λ^0) from the CMS Λ_b^0 Cross Section Analysis [15] was one of the first cross check point for this analysis. The Cross Section Analysis was measured using 1.8 fb^{-1} from the 2011-A dataset and for the HLT displaced J/ψ trigger path:

"HLT_Dimuon7_Jpsi_Displaced / HLT_DoubleMu3p5_Jpsi_Displaced"

whose fiter name is: "hltDisplacedmumuFilterJpsi". The run number associated to this study/dataset is shown in Fig. 5–2. We have then reproduced (right side Fig. 5–3) their

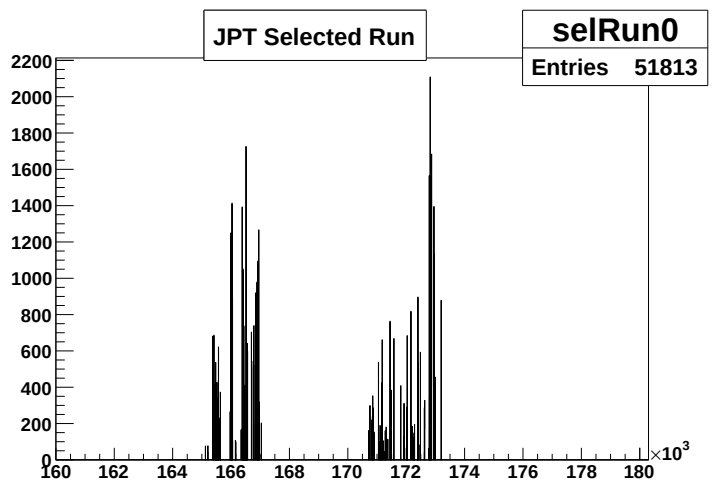

Figure 5–2: Run number used in [15] corresponding to a total integrated L=1.8 fb^{-1}. $\Lambda_b^0 \rightarrow \Lambda^0 J/\psi$ signal (left side Fig. 5–3 rate and Signal/Noise ratio following the same set of cut described in Table 4–4, 4–5 and the kinematics Λ_b^0 cuts of p_t and y which are also used in this analysis with the displaced low dimuon mass trigger. The J/ψ and the Λ^0 has been also reproduced and are shown in Fig. 5–4 A more detailed study was presented at the B Physics group meeting [31].

5.1.2 Appendix B: Split Sample (Run 2011 A vs B)

Figs. 5–5 and 5–6 show the signal and the normalization mode as a function of the run dataset fitted according to the PDF model using Extended Unbinned Maximum Likelihood method with a double gaussian function with the same mean each to describe

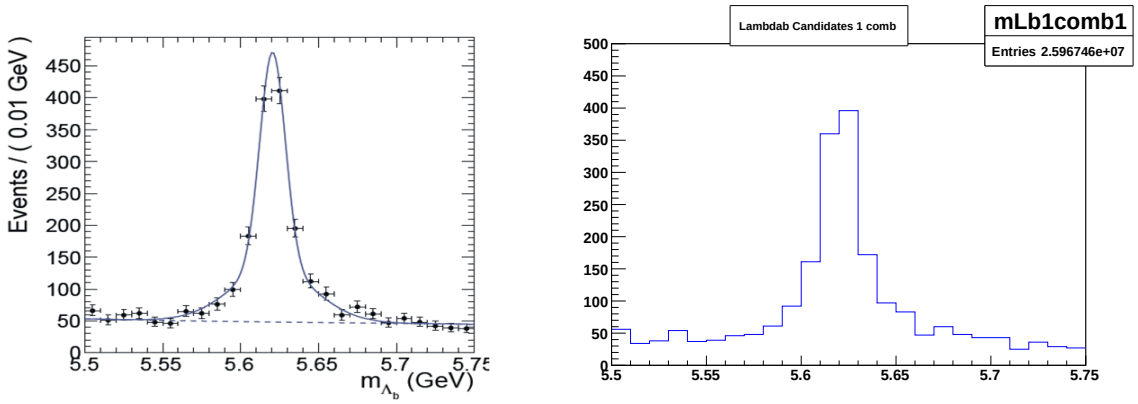

Figure 5–3: $\Lambda_b^0 \to \Lambda^0 J/\psi$ sample from [15] (left) and this analysis (right).

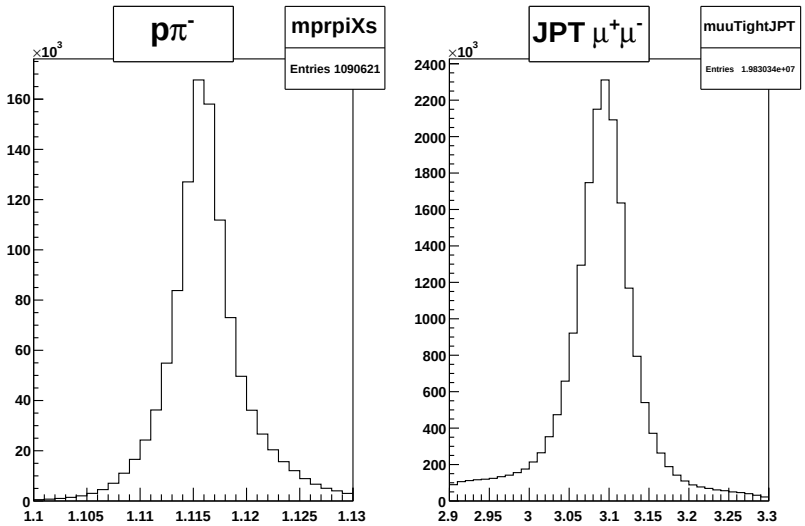

Figure 5–4: J/ψ and Λ^0 in this analysis.

the signal peak and a second degree Chevycheb Polynomial function for the background. The yield for these signal are in the statistical box of each histograms and summarized in Table 4–11.

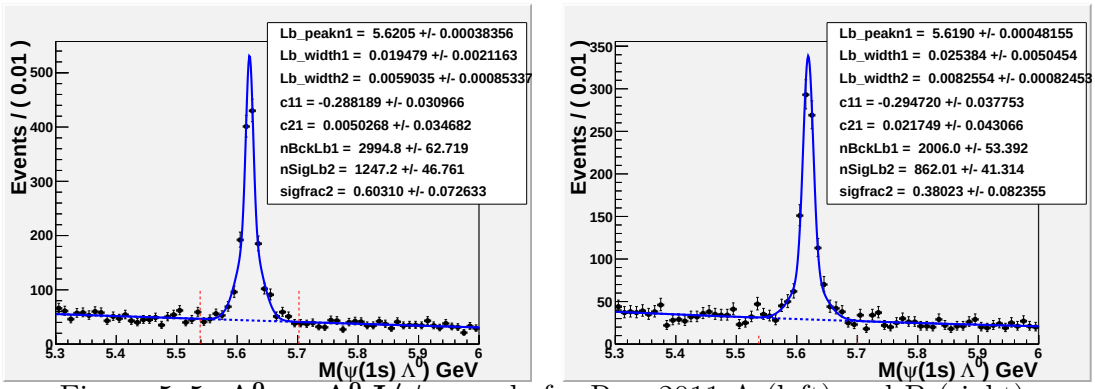

Figure 5–5: $\Lambda_b^0 \to \Lambda^0 J/\psi$ sample for Run 2011 A (left) and B (right).

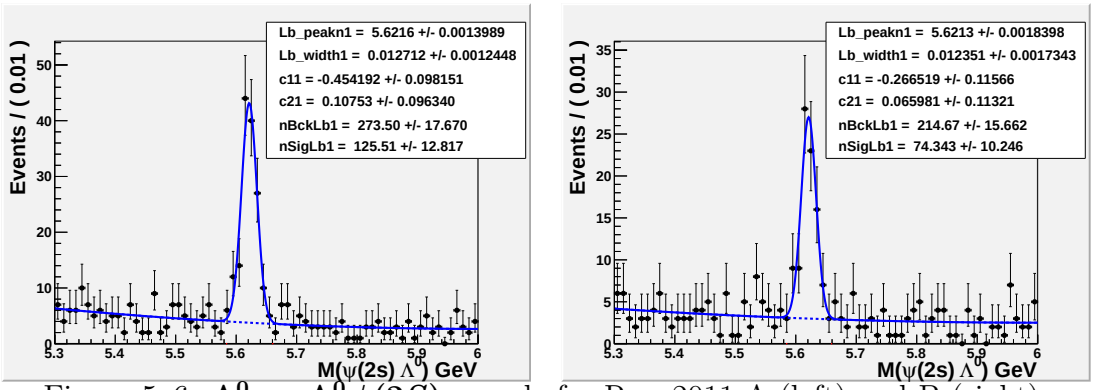

Figure 5–6: $\Lambda_b^0 \to \Lambda^0 \psi(2S)$ sample for Run 2011 A (left) and B (right).

REFERENCES

[1] Science for Scientists. *Tag Archives: god particle*. http://scienceforscientists.wordpress.com/tag/god-particle/.

[2] Kurt Brendlinger. *Recent Higgs Results from the ATLAS experiment*. http://www.dsu.edu/research/ppc2013/talks/2013/Talk-9-Kurt.pdf.

[3] ATLAS Experiment. *The Penguin Domination*. http://atlas.ch/blog/?tag=decay-channels.

[4] European Organization for the Nuclear Research CERN. *sLHC*. http://project-slhc.web.cern.ch/project-slhc.

[5] N.A.Kruglov L.I.Sarycheva I.N.Vardanyan A.A.Yershov. A.I.Demianov, A.M.Gribushin. *CMS (Compact Muon Solenoid)*. http://lav01.sinp.msu.ru/experiments.html.

[6] Wikipedia. *Compact Muon Solenoid*. http://en.wikipedia.org/wiki/Compact_Muon_Solenoid.

[7] UCLA Collider Physics. *CSC Strip, Wire, and Chamber Orientation*. http://www-collider.physics.ucla.edu/cms/trigger/orient.html.

[8] Paolo Azzurri. *The CMS Silicon Strip Tracker*. http://arxiv.org/pdf/physics/0512097.pdf.

[9] Linear Collider COllaboration. *CMS Solenoid*. http://newsline.linearcollider.org/2011/05/05/one-hundred-years-of-superconductivity/cms-solenoid-magnet/.

[10] S. Marcellini. *The Muon System of the CMS Experiment at LHC*. http://particles.ipm.ir/conferences/FIMLHCP/Lectures/S.%20Marcellini.pdf.

[11] European Organization for Nuclear Research CERN. *Muon Detectors*. http://cms.web.cern.ch/news/muon-detectors.

[12] Maxime Gouzevitch. *des Premires Donns*. https://www.ipnl.in2p3.fr/IMG/pdf/20100302_Lyon.pdf.

[13] Katja Klein. *The CMS Silicon Strip Tracker - Overview and Status*. http://web.physik.rwth-aachen.de/~klein/eps_proc.pdf.

[14] European Organization for Nuclear Research CERN. *Silicon Pixels*. http://cms.web.cern.ch/news/silicon-pixels.

[15] K. Ulmer *et al.* Measurement of Λ_b^0 production in pp collisions at $\sqrt{s} = 7$ TeV. CMS Internal Note 2011/434, 2012. http://cms.cern.ch/iCMS/jsp/openfile.jsp?tp=draft&files=AN2011_434_v7.pdf.

[16] R. Michael Barnett. *The Charm of the Strange Quarks*. Springer, first edition, 2000.

[17] D. Griffiths. *Introduction to elementary particles*. Addison-Wessley, first edition, 1987.

[18] S. F. Novaes. *Standard Model: An Introduction*. arXiv:hep-ph/0001283v1, 1999.

[19] Gordon McCabe John. *The structure and interpretation of the standard model*. John Wiley and Sons, first edition, 2007.

[20] IOP Science. *The CMS experiment at the CERN LHC*. http://iopscience.iop.org/1748-0221/3/08/S08004, 2008.

[21] Lyndon Evans and Philip Bryant. *LHC Machine*. Institute of Physics and SISSA, 2008.

[22] The free enciclopedia Wikipedia. *CMS experiment*. http://en/wikipedia/org/wikiCompact_Muon_Solenoid, 2011.

[23] CMS Collaboration. *CMS Design Technical design support Volume I: Detector performance and software*. CERN/LHCC 2006-001, first edition, 2006.

[24] P. Chang. *Workshop on LHC Physics and the Strategies for Discovery*. First edition, 2008.

[25] CMS Collaboration. *Technical Proposal for the Upgrade of the CMS Detector Through 2020*. Technical design report, 2011.

[26] Europhysics letters EPL. *Pseudorapidity distributions of produced charged hadrons in pp collisions at RHIC and LHC energies.* http://iopscience.iop.org/0295-5075/95/6/61001, 2011.

[27] M. Kraemer J. G. Koerner, D. Pirjol. *Heavy baryons.* http://arxiv.org/pdf/hep-ph/9406359v1.pdf, 1994.

[28] J. Beringer *et al.* Review of particle physics and 2013 partial update for the 2014 edition. *Phys. Rev. D*, D86(010001), 2012.

[29] M. Dinardo *et al.* Angular Analysis and differential branching fraction of the decay $\mathrm{B}^{\mathbf{0}} \rightarrow \boldsymbol{K^{*0}\mu^{+}\mu^{-}}$. CMS Internal Note 2012/119, 2012. http://cms.cern.ch:80/iCMS/analysisadmin/get?analysis=BPH-11-009-pas-v0.pdf.

[30] H Woehri. Evolution of muon trigger menu. https://espace.cern.ch/cms-quarkonia/trigger-bph/default.aspx.

[31] H Mendez. Progress report on BR($\boldsymbol{\Lambda_b^0 \rightarrow \Lambda^0 \psi(2s)}$). https://indico.cern.ch/conferenceDisplay.py?confId=259423, Jul 10 2013. B physics PAG meeting.

[32] MuonPOG. Baseline muon selections. https://twiki.cern.ch/twiki/bin/view/CMSPublic/SWGuideMuonId#Tight_Muon.

[33] H Mendez. $\boldsymbol{\Lambda_b^0 \rightarrow \Lambda^0 \psi(2s)}$. https://indico.cern.ch/conferenceDisplay.py?confId=288572, Dec 18 2013. B physics WG meeting.

[34] M. Falla. Analysis of a $\boldsymbol{\Lambda_b^0}$ decay mode, May 2 2013. Msc. Thesis work, University of Puerto Rico - Mayaguez, Physics Dept.

[35] Paul Avery. *Particle Decay Rates, Lifetimes and Branching fractions.* http://www.phys.ufl.edu/~avery/course/4390/f2013/lectures/particle_width_rate_lifetime.pdf, 2013.

[36] CMS Twiki. *Public CMS Luminosity Information.* https://twiki.cern.ch/twiki/bin/view/CMSPublic/LumiPublicResults, 2014.